MODELING OF ELECTROMAGNETIC, HEAT TRANSFER, AND FLUID FLOW PHENOMENA IN AN EM STIRRED MELT DURING SOLIDIFICATION

by

GREGORY MICHAEL POOLE

NAGY EL-KADDAH, COMMITTEE CHAIR
LAURENTIU NASTAC
MARK L. WEAVER
HEATH TURNER

A THESIS

Submitted in partial fulfillment of the requirements
for the degree of Master of Science in the
Department of Metallurgical and Materials Engineering
in the Graduate School of
The University of Alabama

TUSCALOOSA, ALABAMA

2013

ABSTRACT

A methodology is presented to simulate the electromagnetic, heat transfer, and fluid flow phenomena for two dimensional electromagnetic solidification processes. For computation of the electromagnetic field, the model utilizes the mutual inductance technique to limit the solution domain to the molten metal and magnetic shields, commonly present in solidification systems. The temperature and velocity fields were solved using the control volume method in the metal domain. The developed model employs a two domain formulation for the mushy zone. Mathematical formulations are presented for turbulent flow in the bulk liquid and the suspended particle region, along with rheological behavior. An expression has been developed—for the first time—to describe damping of the flow in the suspended particle region as a result of the interactions between the particles and the turbulent eddies. The flow in the fixed particle region is described using Darcy's law. Calculations were carried out for globular and dendritic solidification morphologies of an electromagnetically-stirred melt in a bottom-chill mold. The coherency solid fraction for the globular solidification morphology was taken to be 0.5, while the coherency for dendritic morphology was 0.25. The results showed the flow intensity in the suspended particle region was reduced by an order of magnitude. The effect of the heat extraction rate on solidification time was investigated using three different heat transfer coefficients. The results showed that the decrease in solidification time is nonlinear with respect to increasing heat transfer coefficient. The influence of the final grain size on the damping of the

flow in the suspended particle region was examined, and it was found that larger grain sizes reduce the extent of flow damping.

LIST OF ABBREVIATIONS AND SYMBOLS

A	Magnetic vector potential
A_p	Particle surface area
a_i	Matrix coefficients
B	Magnetic flux density
C_1	Turbulence constant
C_2	Turbulence constant
C_μ	Drag coefficient
C^*	Apparent heat capacity
c_p	Specific heat
c_p^l	Liquid specific heat
c_p^s	Solid specific heat
D_g	Final grain size
d_g	Instantaneous grain size
D_i	Conductance

$d\mathbf{l}$	Differential line element
$\mathbf{E}$	Electric field
EM	Electromagnetic
$\mathbf{F}_b$	Bouyancy force
$\mathbf{F}_{em}$	Lorentz force
$\mathbf{F}_d$	Damping force
F_i	Convective flux
f_c	Coherency solid fraction
f_l	Liquid fraction
f_s	Solid fraction
G_{ij}	Turbulent shear generation
$\mathbf{g}$	Gravitational vector
H	Height of the metal
h	Heat transfer coefficient
$\mathbf{I}$	Unit tensor
I_T	Turbulent intensity
$\mathbf{J}$	Current density vector

j	Square root of -1
K	Flow permeability
k	Turbulent kinetic energy
k_e	Effective thermal conductivity
k_s	Thermal conductivity of the solid
k_l	Thermal conductivity of the liquid
L	Latent heat of fusion
M_{ij}	Mutual inductance
N	Number of grains in control volume
n	Grain growth exponent
ñ	Unit surface normal
P	Pressure
Pr	Prandtl number
q	Heat flux
r	Position vector
r'	Source position vector
R	Radius of metal specimen

R_T Turbulent Reynolds number

S Surface normal

S_{em} Electrical energy dissipation

S_L Latent heat source term

Su Matrix source term

Sp Linearized source term

T Temperature

T_0 Reference temperature

T_∞ Ambient temperature

T_L Liquidus temperature

T_S Solidus temperature

T_{coh} Coherency temperature

t Time

u Velocity vector

u Axial velocity component

u’ Turbulent fluctuating velocity

V Volume

v	Radial velocity component
∇	Del operator
β	Volume coefficient of thermal expansion
Γ_ϕ	General diffusion coefficient
ε	Turbulent energy dissipation
ρ	Density
ρ_0	Reference density
μ_0	Permeability of free space
μ_0^*	Molecular viscosity
μ_l^*	Effective laminar viscosity
μ_t	Turbulent viscosity
ϕ	General transport variable
σ	Electrical conductivity
σ_k	Turbulent Prandtl number for k
σ_k	Turbulent Prandtl number for ε
$\boldsymbol{\tau_t}$	Turbulent (Reynolds) Stress

ACKNOWLEDGEMENTS

I would first like to express my gratitude to my advisor, Dr. Nagy El-Kaddah, for sharing his seemingly boundless knowledge and for spending countless hours helping me analyze the results contained in this work. I would also like to thank the National Science Foundation for giving me the great privilege to carry out this study under grant number CMMI-0856320; furthermore, I would like to thank the members of my defense committee, Drs. Laurentiu Nastac, Mark L. Weaver, and Heath Turner, for taking the time to offer their insights and suggestions on this project.

In addition to those who have been instrumental in offering their guidance in this work, prudence dictates that gratitude be expressed for those who have made indelible impressions on my career. In this regard, I must offer thanks to my high school mathematics teachers, Ms. Vanetta Clark, Mrs. Betty Trayvick, and Mrs. Elaine Noland, whose instruction inspired me to gain and apply my mathematical knowledge to the benefit of society. I would also like to thank David Nikles, Professor of Chemistry at the University of Alabama, who opened the possibility of me becoming a professional scientist by allowing me to work with him on his research with the Center for Materials for Information Technology. Most importantly, I thank my father, Michael, and my mother, Susan, for supporting my endless quest for knowledge.

Finally, I extol the highest praise to God, from whom all of these blessings and opportunities flowed. May this work forever glorify Him.

CONTENTS

LIST OF TABLES

LIST OF FIGURES

CHAPTER 1

INTRODUCTION

Electromagnetic induction stirring is widely used in many solidification processes as a means to produce a fine grain structure. In induction stirring, an external coil induces a current inside the molten metal; the eddy currents interact with the magnetic field to produce stirring (Lorentz) forces which drive the fluid flow. The flow field is typically very intense and highly turbulent [1]; as a result, convective phenomena tends to dominate their diffusive counterparts in the microstructure and macrostructure evolution during solidification. This ability to produce such an action at a distance makes electromagnetic stirring unique in its adaptability to a number of casting and solidification processes. Example processes include continuous casting [2], rheocasting [3], and electroslag remelting [4].

The role of the flow on solidification structure evolution is manifold. In the bulk liquid, the flow rapidly dissipates the superheat and homogenizes the temperature and solute fields [5-6], resulting in uniform growth kinetics and a uniform grain structure [7]. The flow also increases the local partition coefficient at the solid/liquid interface [8-9] and lowers the temperature gradient at the interface [10], leading to less microsegregation and greater amounts of constitutional undercooling just ahead of the advancing solidification front [11-12]. The combination of these bulk and interfacial phenomena contribute to increased generation and survival of nuclei [13-14] and the promotion of the columnar-to-equiaxed transition [15].

Electromagnetic stirring also significantly promotes dendrite fragmentation—first proposed by Jackson and associates [16], and later verified in various in-situ experiments for both metal and transparent model alloy systems [17-19]. As explained by Dantzig and Rappaz [20], flow within the coalesced interdendritic region transports solute-enriched liquid to the solid/liquid interface. As a result, dendrite tips in the surface layer undergo solutal remelting and detach; the bulk flow then advects these fragments into the liquid, further increasing the nucleation potential in the undercooled region.

It is therefore clearly apparent that thoroughly understanding the flow characteristics in the two-phase (mushy) region would provide appreciable insight on the development of these phenomena. One particular method—mathematical modeling—provides an alternative to extensive experimentation to provide this understanding; however, modeling is only useful to the extent that the physical phenomena are accurately defined. It is imperative that all aspects of the flow in the bulk liquid and in the mushy zone be accounted for if a realistic solution is to be obtained [21].

A number of approaches have been developed to this effect. Initial efforts involved treating the mushy zone as a porous medium [22-26]. To this effect, Darcy's law was used to damp the momentum over the entire mushy zone, and the permeability was most commonly described by the Carman-Kozeny relation [27]. Analysis of the experimental data has led to empirical relations describing the characteristic pore size to the primary or secondary dendrite arm spacing [28]. In general a majority of previous studies using stationary particle models are for either buoyancy or shrinkage-driven flows; it is important to note, however, that there were some efforts to incorporate turbulence for cases involving forced convection [29-31]

Experimental observations have shown, however, that the flow only exhibits Darcian behavior at higher values of solid fraction [31-33], which negates the validity of the porous bed assumption over the entire mushy zone. Oldenburg and Spera sought to account for this drawback by relaxing the packed bed assumption for low solid fraction and substituting a two region model [35]. A homogeneous model was used to describe the flow in the suspended particle region, and the viscosity of the solid-liquid mixture was described by rheological behavior. Beckermann and coworkers used a volume-averaged two-phase flow model to determine the velocities of both the liquid and the solid in this region [36-38], and Nikrityuk et al applied rheological behavior over the entire mushy zone [39]. These models assumed laminar flow in the bulk liquid and mushy zones. Recently, Pardeshi et al extended the hybrid model to describe solidification in the presence of turbulent flow [40]. They used the k-ε model to describe the turbulent characteristics in the bulk liquid and in the suspended particle region. However, the model does not account for damping of the flow by particle interactions with the turbulent eddies. The dissipation of turbulent kinetic energy at the solid surfaces plays a key role in damping the flow in the liquid phase, and should be considered in the analysis to accurately predict the liquid velocity.

The purpose of this work is to develop a comprehensive model for EM stirring in solidification processes. The goals are as follows:

(a) To fundamentally describe the turbulent interactions with the crystallites in damping the flow in the mushy zone.

(b) To develop a solution methodology for solving the coupled electromagnetic field, temperature, and turbulent fluid flow equations in solidification processes.

(c) To investigate the influence of crystallite size and solidification morphology on the fluid flow—in both the bulk liquid and mushy zone—and solidification behavior during unidirectional solidification in a bottom chill mold.

The thesis shall proceed in the following sequence. Chapter two will provide a review of relevant literature, while Chapter three will present a solution methodology and associated equations for computing the electromagnetic, temperature, and turbulent velocity fields. Chapter four will present the results along with a detailed discussion, and Chapter five will briefly review the principal findings of this work and suggest future research endeavors.

CHAPTER 2

LITERATURE REVIEW

In recent decades, significant strides have been made in the simulation of fluid flow, heat transfer, and mass transfer phenomena in solidification processes as well as electromagnetic phenomena in electromagnetic material processing systems. This chapter will provide a recounting of previously published literature on numerical simulation of the electromagnetic, temperature, and velocity fields in solidification systems.

2.1 Computational Electromagnetics

The electromagnetic field in EM stirring applications is typically produced using a suitable induction coil and is represented by the well-known Maxwell equations [41]. In essence, these equations are the differential formulation of the integral Gauss laws for conservation of electric and magnetic fields, Ampere's law, which relates the electric current to the magnetic field, and Faraday's law of induction.

Most computational techniques for calculating the EM field are based on solution of the differential form of the Maxwell equations using potential formulations for the electric field, **E**, and magnetic field, **B**. This is done to simplify the handling of the boundary conditions and discontinuities in the tangential component of the electric field and the normal component of the magnetic field. Potentials may be classified as scalar potentials or vector potentials. The most common scalar potentials used in formulating alternating EM field problems are the electric

scalar potential, V, and the reduced magnetic scalar potential, Ψ. Along the same lines, the most common vector potentials are the current vector potential, **T** , and the magnetic vector potential, **A**. The scalar potential equations are the Laplace-Poisson type, while the governing vector potential equations are classified as diffusion-type for time-varying EM fields.

A clear majority of formulations for eddy current problems have been based on the magnetic vector potential, with the current vector potential coming into use more recently. Roger and Eastham [42] used the vector potential **A** for the field conductor and scalar potentials—Ψ for free space and ϕ for ferromagnetic materials—in non-conducting media. The source field was given via the Biot-Savart law. The formulation is only applicable for singly-connected conducting domains with uniform electrical conductivity. Furthermore, it must be assumed that the induced field does not affect the source field. Pillsbury [43] introduced the **A**,V-ϕ formulation to allow for variable electrical conductivity. In this formulation, the magnetic and electric fields in the conducting region are determined by solving for **A** and V, respectively, with ϕ being solved in free space. The use of the magnetic scalar potential in free space, however, still means that the Pillsbury formulation may not be used for multiply-connected domains. Roger et al [44] proposed using cuts in the conductor in the direction of the current as a remedy to this drawback, but implementation requires special routines to deal with the discontinuities at the cutting surfaces, increasing the computational complexity of the problem. To handle the field in multiply-connected conducting domains, Chari et al [45] and Biddlecombe et al [46] proposed the **A**,V-**A** formulation. This allows for the solution domain to have multiple conductors in the domain and relaxes the need for stiff current sources, at the cost of increased degrees of freedom.

The current vector potential formulation was first suggested by Carpenter et al [47-49], and the **T**-Ψ,Ψ formulation was first used by Preston et al [50]. In these formulations, the current vector potential is used to solve for the eddy current distribution within the conductor, while the magnetic field is represented by its reduced scalar potential. A Coulomb gauge was employed to enforce continuity of **T** at the boundaries. This continuity means that the formulation can be used for multiply-connected domains. The computational advantages associated with the various magnetic vector potential and current vector potential formulations were investigated by Reinhart et al [51] and Biro et al [52].

Solutions of the differential equations are typically carried out using the finite element method (FEM), finite difference method (FDM), or control volume (CV) techniques. The reader may refer to the following References [53-55] for the detailed these methods. The principal drawback associated with these solution methods lies in the fact that eddy current problems are open boundary ones. This means that the solution domain must not only include the conducting regions(s) of interest, but also of free space in order to define the boundary conditions of the solution domain, leading to a significant decrease in computational efficiency. This hindrance may be remedied through the use of hybrid techniques which utilize two different solution methods in such a way that the weakness of one method is complemented by the strength of its counterpart. In the hybrid boundary element/FEM technique of Salon [56], the differential vector potential equations are solved using FEM within the conductor, while the boundary conditions are satisfied using the boundary element method. El-Kaddah and coworkers [57] introduced the CV/integral method. In this procedure, the CV technique is used to solve the magnetic diffusion equation in the conductor and the field at the boundary is resolved using the Biot-Savart law. An analogous procedure was developed using the finite element method [58]. Later work showed

that these hybrid methods were more computationally efficient than any of the standalone solution methods [59].

For two-dimensional systems, it is advantageous to solve the electromagnetic field problem using an integral formulation. This is typically done using the mutual inductance method first proposed by Kolbe and Reiss [60] and applied by Dudley and Burke [61]. In this technique, the system is divided into a number of elementary circuits whose volume elements are assumed to possess constant current density. Using this assumption, the eddy currents in each circuit may be expressed in terms of the contributions of all other circuits in the system. This resulting set of simultaneous equation may be readily solved to yield the current distribution. Relations for calculating the self-inductance and mutual inductance may be found in electrical engineering textbooks [62]. In addition to its simplicity, the mutual inductance method allows for the solution of the EM field in multiply-connected arbitrary domains and avoids the need to grid free space. This method was extensively used for modeling material processing systems including, but not limited to, induction furnaces [63], electromagnetic casting of aluminum [64], and EM stirring systems [5,7,65].

2.2 Modeling of Solidification Processes

Solidification is a classical moving boundary problem and encompasses transfer of heat, mass, and momentum (fluid flow). Development of mathematical modeling tools to describe solidification processes, which involve the solution of governing heat, mass, and momentum equations, are of paramount importance in order to obtain a vivid understanding of solidification phenomena.

2.2.1 Solidification in Stagnant Fluids

Initial efforts to develop a mathematical description of solidification processes were focused on idealized problems assuming no convection in the liquid phases (i.e. stagnant liquid) and pure materials. Such studies were later expanded to include alloy systems.

2.2.1.1 Solidification of Pure Metals

A well-known class of one dimensional solidification problems involving pure materials is the Stefan problem. Solution of these problems requires the determination of the temperature profile in each phase via solution of the respective conservation equations, and knowledge of the rate of solidification front advancement, in order to resolve the Helmholtz conditions at the interface.

Early solutions of these types of problems in one dimension were exact analytical in form. The most renowned analytical solution is that of Neumann [66], who solved the problem for unidirectional solidification in a semi-infinite medium using a similarity approach, transforming the partial differential equations into ordinary ones. This is necessary due to the non-linear nature of the energy balance at the interface. Similar solutions for radially symmetric systems with centered line (or point) source/sink terms may be found in the work of Frank [67].

However, the assumptions and simplifications involved in obtaining an exact solution limit their applicability with regards to bounded systems [68, 69], requiring approximate integral methods instead. The method of Goodman [70] assumed a solid temperature fixed at the melting point and a quadratic temperature distribution in the liquid. Lightfoot [71] examined the unidirectional solidification of steel by treating the latent heat released as a moving heat source. This approach was extended to two space coordinates by Rathjen and Jiji [72] for freezing of a

corner section and Budhia and Kreith [73] for solidification of a wedge. Although these methods do allow for semi-analytical solutions for bounded systems, they still require a number of simplifications. For more information on analytical methods for Stefan problems, see Rubinstein [74].

The drawbacks of the analytical methods mentioned above have led to the development of numerical solutions for Stefan problems in multiple space coordinates. Pure materials undergo isothermal phase transformation and feature a sharp, distinct interface. This discontinuity may be treated using front-tracking, boundary immobilization, or specific heat methods.

In the front-tracking approach first introduced by Murray and Landis [75], the grid features a set of marker nodes to explicitly define the interface location, and are connected using a piecewise function—typically a polynomial. While the grid far from the moving boundary is fixed and regular, the grids adjacent to the solidification front are deformed and irregular in nature. In the work by Unverdi and Tryggvason [76], an indicator function was used to define the interface by assigning integer values to each phase. The marker nodes, defined by an interpolant, were allowed to propagate through a fixed grid. While this method is useful in many one and two-dimensional problems, issues arise when dealing with three-dimensional systems with asymmetric interfaces. The level set method, developed by Osher and Sethian [77], easily handles these complex geometries. The method relies on the determination of a level set function that satisfies a Hamilton-Jacobi equation, where the interface is defined as the zero level set. Implementation, however, is computationally expensive, as the level set method requires a very fine grid structure to accurately define the interface.

In boundary immobilization methods, the governing heat conduction equation and the boundary conditions are transformed into a non-orthogonal coordinate space. The interface in this new coordinate system lies on a single, fixed coordinate surface with mobile outer boundaries, making this a Lagrangian solution method. This method was first used for sharp interfaces by Crank [78], and extended to two-dimensions by Duda et al [79] for phase change of a finite, bounded cylinder. In the work by Saitoh [80], the system was mapped using the Landau transformation, thereby reducing the number of space variables by one. Each of these studies used the finite difference method to achieve solution. Hsu et al [81], on the other hand, used the control volume technique to solve the transformed equations. Although the boundary immobilization method has been shown to produce accurate solutions of benchmark problems [82], the transformed conservation equations contain highly nonlinear cross-derivative terms consisting of more than one space variable, which make implementation cumbersome.

The specific heat method, first introduced by Thionov and Samarskii [83], seeks to avoid the need to explicitly discretize the boundary by introducing an effective specific heat capacity near the transformation temperature. This is accomplished by assuming that the discontinuity in enthalpy can be represented by a very narrow freezing range. This allows for the heat conduction equation to be rewritten in terms of a piecewise function to represent the specific heat. A thorough introduction to the method, along with examples, may be found in Szekely and Thelimis [84]. The first applications of this method comes from Soviet literature via the works of Budak et al [85] and Samarskii and Moisyenko [86] for generalized Stefan problems. For pure materials, the latent heat evolution is assumed to be linear with respect to temperature.

2.2.1.2 Solidification of Alloys

In alloy systems, the phase transition is not isothermal, but rather occurs over a temperature range, the extent of which may be ascertained through use of a phase diagram. Alloy solidification begins at the liquidus temperature, and may be regarded as complete at the solidus temperature. The incremental nature of this phase change makes application of front-tracking and boundary immobilization methods impractical.

For alloy solidification, latent heat evolution is depended on transformation kinetics. At the macro-level, this can be represented through the rate of change of solid fraction, which is typically given as a function of temperature. This allows for the use of the specific heat method [87]. A number of functions have been developed to represent the solid fraction. The simplest is assuming the solid fraction obeys a linear relationship with temperature, and is used in the works of Voller and Prakash [24] and Poole et al [88], among others. For equilibrium solidification with solute segregation, the lever rule is used [89]; the partition coefficient is assumed constant for nearly-linear solidus and liquidus lines. For non-equilibrium solidification, the Schiel equation is typically used [90]. In addition, the solid fraction may also be defined as a piecewise function using experimental solidification curves. Examples of this method are given in Carlson and Beckermann [91] and Li et al [92].

2.2.2 Solidification Models with Fluid Flow

The stagnant fluid assumption from early formulations makes for a simpler solution of solidification problems. Experimental observations, however, make validity of this assumption rare, as the presence of fluid flow and convective heat and mass transfer causes significant deviation from diffusion-only solutions. Such convective phenomena have been shown to have a

strong influence on the microstructure and segregation profiles of the final product [5-10, 15, 17-20, 93].

Convective transport is generally categorized into two regimes: natural convection and forced convection. In natural convection, fluid flow occurs as a result of density differences stemming from thermal gradients in the liquid and solute rejection at the interface. The intensity of natural convection is defined by the Rayleigh number, which describes the relative strength of the buoyancy and viscous forces. Theoretical studies [94-96] determined the critical value of the Rayleigh number for the onset of natural convection in alloys to be on the order of 10^4. Experimental work [97-99] found that convection in aqueous alloy analogues significantly alters the solidification velocity and the curvature of the melt front, both important parameters in determining the solidification morphology and grain size [100]. The work by Stewart [101] using radioactive tracers in the Al-Ag alloy system found natural convection to play a substantial role in macrosegregation.

Forced convection occurs through application of body forces via an external source which may be mechanical [102], ultrasonic [103], or electromagnetic [1-5] in form. The effects of forced convection on the micro/macrostructure are well-documented. Liu et al [104] found that forced convection homogenized the alloying elements in the liquid and improved solution strengthening of AZ91 magnesium specimens. Kuznetzov [105] found considerable inverse segregation of carbon in twin-roll cast steels. Most important is the role of stirring on grain refinement through dendrite fragmentation and transport, which increases the nucleation potential in the melt [15-20].

It is important to note that convection, regardless of the source, is found not only in the bulk liquid, but in the mushy zone as well [32-34, 106]. Several formulations characterizing the flow in the mushy zone have been developed, and may be fundamentally classified as either single-zone or dual-zone models.

2.2.2.1 Single-Zone Models

The first single-zone model was that by Mehrabian et al [107] to describe the role of interdendritic flow on solute redistribution. The entire mushy zone was assumed to behave as a porous medium that obeys Darcy's law, with the permeability given by the Hagen-Poiseuille relation. Although the model was found to be in agreement with experimental work with ternary alloys [108], the solution domain was limited to the mushy zone only. Szekely and Jassal [109] later expanded the solution domain to include both the bulk liquid and the mushy zone.

The extent of momentum damping in Darcy flows is dependent on the permeability of the medium, which is expressed in terms of the flow intensity and the geometry of the interdendritic network. For macro-scale models, the permeability is taken as isotropic due to the randomness of the dendrite orientations [110]. A number of permeability models have been proposed. The Hagen-Poiseuille model describes the permeability through friction loss in laminar flow through a tube [111], and is a good approximation for columnar solidification. The Hagen model was commonly used in the works of Mehrabian and his coworkers [22, 23, 108] and by Poirier and coworkers [112-114]. For equiaxed and globular morphologies, the permeability is most commonly given by the Kozeny family of equations (e.g. Carman-Kozeny [27] and Blake-Kozeny [112]). These assume laminar flow through array of packed spheres. Kozeny

relationships may be found in Voller and Prakash [24], Incropera and coworkers [25,30], and Campanella et al [26], among many others.

Due to the irregular nature of dendrites, analyses correlating the permeability to the dendrite arm spacing have been performed. Poirier [28] did a regression analysis of the data from experimental permeability measurements (see References [33,34,115,116]), and expressed the Hagen-Poiseuille and Blake-Kozeny equations in terms of the primary dendrite arm spacing and a coefficient dependent on the grain tortuosity. The tortuosity has been described in terms of a power series with respect to the ratio of the primary arm spacing to its secondary counterpart [117], or in terms of a shape factor [118].

The previously-mentioned single-zone models were for laminar flow only. There have been some efforts to account for turbulence in the mushy zone. Shyy et al [29] were the first to incorporate turbulence in the single-zone model. To account for the effect of momentum damping on the turbulent characteristics of the flow, a k-ε model for low Reynolds number flows was used. However, the formulation did not account for the added dissipation due to interaction between the turbulent eddies and the solid phase [119], and only gave the turbulence constant C_μ a functional dependence, leaving the constants associated with the source and sink terms unchanged from that for bulk flow. This ad-hoc approach prevents turbulent closure of k and ε. Prescott and Incropera [30] later attempted to define the turbulent flow field for an EM stirred system using the k-ε model of Jones and Launder [120], and reported significant damping of turbulence in the mushy zone. Although turbulent closure is attained, the researchers incorporate a Darcy term in the k and ε equations that does not reflect the physics of the problem, as Darcy's law only applies to laminar flow. Furthermore, the assumption of turbulent flow in both models is incompatible with the porous medium model, as the turbulent mixing length is larger than the

pore size, which is on the order of microns. Such mixing lengths are on the Kolomogrov scale, making the flow essentially laminar with regards to the macro-scale [121].

2.2.2.2 Dual-Zone Models

While single-zone models have proven useful in describing the interdendritic/mushy zone flow for castings exhibit columnar solidification morphology, use of the porous medium assumption over the entire mushy region is not physically valid for equiaxed solidification structures. Experimental investigations [17,18] have shown that equiaxed crystallites and dendrite fragments may not be regarded as stationary, as assumed in Darcy's law and associated permeability relations, but rather travel with the flow current at low solid fraction. Further work [33,34] has shown that Darcian behavior only occurs at higher solid fractions, where the dendrites have formed an interlocking, immobile mesh.

This presents a need for a dual-zone model to account for the varying behavior of the crystallites with respect to solid fraction. West [122] attempted to account for the behavior of the free crystallites by assuming the existence of two packed bed regions with distinct permeabilities, and was found to be in good agreement with the experimental findings of Piwonka and Flemings [107]. However, this approach still assumes a fixed particle arrangement for the crystallites at low solid fraction, not consistent with the actual physical phenomena, and may not be used for turbulent flow for reasons previously mentioned.

To accurately account for the mobility of free crystallites, the dual-zone formulation of Oldenburg and Spera [35] relaxed the packed bed assumption for the region predominated by free crystallites, forming a suspended particle region. This region, which consists of equiaxed crystallites and fragments, are treated in aggregate using a homogeneous two-phase flow with the

viscosity described by the rheological behavior of slurries. Darcy's law was used for the region where the crystallites have settled and formed a coherent network of stationary particles. The Oldenburg-Spera approach was used by Chang and Stefanescu [123] for modeling of macrosegregation of Al-Cu alloys, and by Mat and Ilegbusi [124,125] for describing macrosegregation in an aqueous alloy analogue under buoyancy-driven flow. This formulation correctly reflects the observed solidification phenomena for equiaxed structures, but is limited only to laminar flow; in contrast, the flow in EM stirred systems is typically turbulent [1,57].

Recently, Pardeshi et al [40] presented a dual-zone formulation that accounts for turbulent behavior in EM stirring systems. In the suspended particle region, the viscosity is given by an empirical relationship, with the Carman-Kozeny relation accounting for the permeability in the fixed particle region. The turbulent characteristics of the flow were determined using the high-Re k-ε model of Launder and Spalding [126] throughout the bulk liquid and the mushy zone. While this represented a significant advancement towards understanding turbulent convective transport in an equiaxed mushy zone, a number of assumptions conflict with physical reality. First, the model suffers from the same mixing length drawback as those of Prescott and Incropera [30] and Shyy et al [29] in calculating the turbulent characteristics in a solidifying porous medium, making turbulent closure unattainable. Furthermore, it does not account for momentum damping, along with laminarization of the flow, in the suspended particle region due to particle interactions with the turbulent eddies. Budenkova et al [31] recently attempted to account for the particle interactions, but used an ad-hoc expression which lacks any physical foundation.

CHAPTER 3

MODEL FORMULATION

This chapter presents a two-dimensional formulation and solution methodology for describing the coupled electromagnetic field, fluid flow, and heat transfer phenomena during solidification in electromagnetically stirred systems.

3.1 Statement of the Problem

Figure 3.1 shows a typical casting system in which the molten metal is stirred by an electromagnetic field. In essence, it consists of a heat extraction device (mold) and an electromagnetic stirrer—typically an induction coil. Heat extraction occurs through the refractory walls, the water-cooled chill plate, or a combination of both. Solidification takes place as a result of heat transfer from the bulk metal to the mold walls. This produces a temperature gradient ranging from the melt temperature to the temperature at the walls, which results in the formation of a solid layer, a liquid layer, and a mushy zone, where the temperature lies between the solidus and liquidus temperatures and the solid and liquid phases coexist in. The shape and thickness of each individual layer for any given time depends on the structure and magnitude of the flow— which is driven by buoyant and/or electromagnetic (Lorentz) forces resulting from

density gradients and the interaction between the current and magnetic field generated by the induction coil in the system, respectively.

In order to develop a fundamental understanding of the solidification phenomena in the mold, one needs to describe the temperature, velocity, and electromagnetic fields. This requires calculation of the electromagnetic field over the entire system, the temperature field in the metal, and the velocity field in both the bulk liquid and the mushy zone.

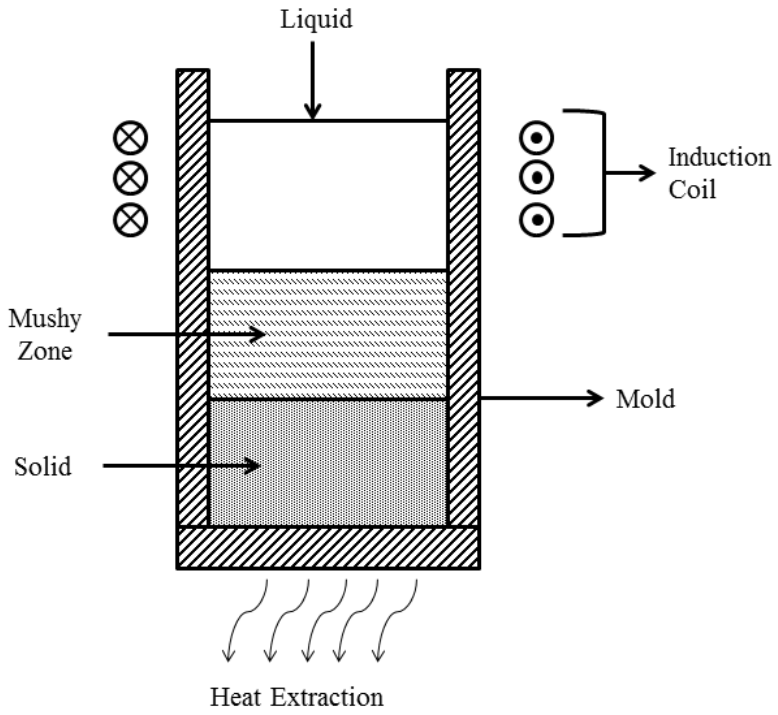

Figure 3.1. Sketch of EM stirred melt undergoing solidification

3.1.1 The Electromagnetic Field Problem

The system shown in Figure 3.1 is just a simple example of an EM stirred system; however, the principles are the same for any two-dimensional EM stirred solidification system. Eddy currents are generated by passing a current through the induction coil, which interacts with the accompanying magnetic field, creating Lorentz forces in the liquid; the rotational part of

these forces drive fluid motion in the molten metal. Furthermore, the eddy currents generate heat through electrical energy dissipation. It is important to note, however, that the magnetic field characteristics depend not only on interactions with the metal, but with adjacent conducting materials such as the chill block and/or magnetic shields. These additional components must be considered in any analysis of the electromagnetic field phenomena.

3.1.2 Heat Transfer Problem

Solidification occurs by heat extraction through the water-cooled chill block located at the base of the metal specimen. The metal is jacketed by a refractory tube, minimizing heat losses from the sides allowing for unidirectional solidification. In the developed model, the metal is represented by three distinct domains: the bulk liquid, the mushy zone, and the solid. Unlike quiescent melts, heat transfer in the bulk liquid is not limited to conduction only, but occurs by convection as well. In the mushy zone, both transport modes still persist, albeit with additional release of latent heat whose evolution depends on the solid fraction, f_s. Upon complete solidification, heat transfer is restricted to conduction only.

3.1.3 Fluid Flow Problem

The presence of the convective regime in the heat transfer problem by convection necessitates the characterization of the velocity field. While the process of defining the flow in the bulk liquid is well-known, the flow characteristics of the mushy zone are dependent on the interactions between the solid and liquid phases. To describe these interactions, the mushy zone was represented by two distinct regions, as shown in Figure 3.2. At values of low f_s, newly-formed crystallites and dendrite fragments move freely with the flow, forming a slurry, and is referred to as the *suspended particle region*. As the crystallites grow, they settle and coarsen into an interlocking network resembling a packed bed. This is referred to as the *fixed particle region.*

In the suspended particle region, the velocity is damped due to interactions between the turbulent eddies and the solid particles at the liquid-particle interface. In the fixed particle region, damping of the flow occurs due to the existence of an increasingly constricted flow path, which may be described in terms of the permeability. Lorentz forces are also affected. In the suspended particle region, electromagnetic forces are unaffected by the presence of crystallites, but may be neglected in the fixed particle region, as the solid is unable to be deformed by the forces. In this region, the flow is driven by buoyancy effects.

The proceeding sections will define the relevant conservation equations for the electromagnetic, temperature, and velocity fields for each domain, followed by the method of solution for these equations.

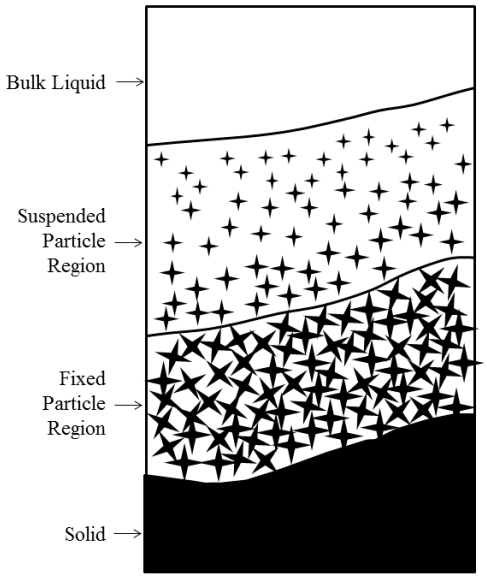

Figure 3.2. Illustration of the various flow domains

3.2 Formulation of the Electromagnetic Field

3.2.1 Governing Equations

The electromagnetic field is governed by the well-known Maxwell equations, which are the differential forms of Ampere's law and Faraday's law, together with constitutive equations describing the relationships between the current, electric field, and magnetic field. Using the magnetohydrostatic assumption—typically appropriate for nonmagnetic materials—Ohm's law is expressed as

$$\boldsymbol{J} = \sigma \boldsymbol{E} \tag{3.1}$$

where σ is the electrical conductivity of the metal, **J** is the current density, and **E** is the electric field intensity. The Lorentz force, $\mathbf{F}_{em}$, may be expressed as

$$\boldsymbol{F_{em}} = \boldsymbol{J} \times \boldsymbol{B} \tag{3.2}$$

where **B** is the magnetic flux density. The electrical energy dissipation (Joule heating) is given in terms of the magnitude of **J** and the conductivity:

$$S_{em} = \frac{J\bar{J}}{\sigma} \tag{3.3}$$

3.2.2 Numerical Solution of the Electromagnetic Field

As previously mentioned in Chapter 2, two common techniques to compute the electric and magnetic fields are differential and mutual inductance methods. In this study, the mutual inductance method was used due to its ability to easily handle the electromagnetic field equations in systems with noncontiguous components.

Due to the axisymmetric nature of the problem shown in Figure 3.1, current flow in the θ-direction, the time-harmonic **J** and **B** fields may be written in phasor form as

$$\boldsymbol{J} = Re\{J_\theta exp[j\omega t]\}\hat{\theta} \tag{3.4}$$

$$\boldsymbol{B} = Re\{\boldsymbol{B} exp[j\omega t + \varphi]\} \tag{3.5}$$

Here, j is the square root of -1, ω is the angular frequency of the inductor, and φ is the phase angle. $\mathbf{F_{em}}$ and S_{em} are given as

$$\boldsymbol{F_{em}} = \frac{1}{2} Re\{\boldsymbol{J} \times \boldsymbol{B}\} \tag{3.6}$$

$$S_{em} = \frac{1}{2} Re\left\{\frac{J\bar{J}}{\sigma}\right\} \tag{3.7}$$

where the bar denotes the complex conjugate of the vector.

The mutual inductance method utilizes the integral form of the Maxwell equations. From Ampere's law the **B** field at **r** due to a current at point **r'** may be given by

$$\boldsymbol{B}(\boldsymbol{r}) = \frac{\mu_0}{4\pi} \oint_{vol} \frac{\boldsymbol{J} \times (\boldsymbol{r} - \boldsymbol{r'})}{|\boldsymbol{r} - \boldsymbol{r'}|^3} dv \tag{3.8}$$

where μ_0 is the magnetic permeability of free space. It is possible to express the previous equation in terms of the magnetic vector potential, **A**, as

$$\boldsymbol{A}(\boldsymbol{r}) = \frac{\mu_0}{4\pi} \oint_{vol} \frac{\boldsymbol{J}}{|\boldsymbol{r} - \boldsymbol{r'}|} dv \tag{3.9}$$

where

$$\boldsymbol{B} = \boldsymbol{\nabla} \times \boldsymbol{A} \tag{3.10}$$

To evaluate **A**, the metal, induction coil, and other conducting components may be subdivided into a number of simple circuits which are assumed to have constant current density. **A** can then be expressed in terms of the individual current densities

$$A_\theta(\boldsymbol{r}) = \frac{\mu_0}{4\pi} \left[\begin{array}{r} \sum_{m=1}^{metal} (\boldsymbol{J}.\boldsymbol{S})_m \oint \frac{\boldsymbol{dl_m}}{|\boldsymbol{r} - \boldsymbol{r'_m}|} + \sum_{c=1}^{cond} (\boldsymbol{J}.\boldsymbol{S})_c \oint \frac{\boldsymbol{dl_c}}{|\boldsymbol{r} - \boldsymbol{r'_c}|} \\ + \sum_{k=1}^{coil} I_k \oint \frac{\boldsymbol{dl_k}}{|\boldsymbol{r} - \boldsymbol{r'_k}|} \end{array} \right] \tag{3.11}$$

where I_k is the applied current in each turn of the induction coil.

Through use of Faraday's law of induction, each individual current, $\mathbf{J}_i$, may be expressed with respect to the current densities in all other elements.

$$\oint \boldsymbol{J}_i . d\boldsymbol{l}_i = -j\omega\sigma \left[\sum_{m=1}^{metal} M_{i,m} (\boldsymbol{J}.\boldsymbol{S})_m + \sum_{c=1}^{cond} M_{i,c} (\boldsymbol{J}.\boldsymbol{S})_c \sum_{k=1}^{coil} M_{i,k} I_k \right] \tag{3.12}$$

where d**l** is the length of the circuit, S is the cross-sectional area of the cell, and $M_{i,k}$ is the mutual inductance given by

$$M_{i,k} = \frac{\mu_0}{4\pi} \oint\oint \frac{d\boldsymbol{l}_k . d\boldsymbol{l}_i}{r\prime} \tag{3.13}$$

Applying Equation (3.12) to the each circuit, a set of simultaneous equations is obtained. The resulting matrix is symmetric and positive definite, and may be solved using Choleski factorization. Upon obtaining the **J** field, Ampere's law is used to obtain **B**.

3.3 Governing Equations for the Heat Transfer Problem

As previously mentioned, the solidification rate depends on the rate of heat extraction from the metal. The differential energy equation is given by

$$\rho c_p \frac{\partial T}{\partial t} + \rho c_p \boldsymbol{u}.\nabla T = \nabla.(k_e \nabla T) + S_{em} + S_L \tag{3.14}$$

where ρ, c_p, and k_e are the density, specific heat capacity, and effective thermal conductivity, respectively, and **u** is the fluid velocity. S_{em} is the electrical energy dissipation per unit volume given in Equation (3.3). S_L corresponds to the release of latent heat and is given as

$$S_L = \rho L \frac{\partial f_s}{\partial t} + \rho L \boldsymbol{u}.\nabla f_s \tag{3.15}$$

where L is the latent heat of fusion. The first term in Equation (3.15) describes the latent heat released due to growth kinetics, while the second term accounts for the latent heat released by advected crystallites. Assuming the linear evolution of solid fraction with respect to temperature, f_s is given by

$$f_s = \begin{cases} 0 & in\ the\ liquid \\ \frac{T_L - T}{T_L - T_S} & in\ the\ mushy\ region \\ 1 & in\ the\ solid \end{cases} \tag{3.16}$$

where T_L is the liquidus temperature and T_S is the solidus temperature. By evaluating the derivatives in the S_L equation, Equation (3.15) can be rewritten as

$$S_L = -\rho \frac{L}{T_L - T_S}\left[\frac{\partial T}{\partial t} + \boldsymbol{u}.\boldsymbol{\nabla} T\right] \tag{3.17}$$

Noting that L/T_L-T_S is the specific heat of fusion and that the bracketed term is the material derivative of T, the conservation equation, Equation (3.14), can be expressed as

$$\rho C^* \frac{DT}{Dt} = \nabla.(k_e \nabla T) + S_{em} \tag{3.18}$$

where C* is the apparent heat capacity, given by

$$C^* = \begin{cases} c_{p,l} & in\ the\ liquid \\ c_{p,l} + \frac{L}{T_L - T_S} & in\ the\ mushy\ zone \\ c_{p,s} & in\ the\ solid \end{cases} \tag{3.19}$$

The effective thermal conductivity depends on the domain. In the solid, the k_e is equal to its molecular value, k_s; for the mushy zone, regardless of region, it is assumed that k_e obeys the following mixture rule:

$$k_e = f_s k_s + (1 - f_s) k_l \tag{3.20}$$

For the bulk liquid, the value of k_e is depends on the turbulent characteristics of the flow, and is given by

$$k_e = k_l + \frac{\mu_t c_{p,l}}{Pr} \tag{3.21}$$

The variables μ_t and Pr correspond to the turbulent viscosity (see Section 3.4) and the Prandtl number, respectively.

3.4 Formulation of the Fluid Flow Model

Since the fluid flow and heat transfer equations are strongly coupled by convection, the velocity must be properly described in both the bulk liquid and mushy zone. Because the flow behavior varies in each domain, each described in Section 3.1.3, this section will describe the models used for each individual domain.

3.4.1 Conservation Equations for Fluid Flow

Fluid flow in the bulk liquid is given by the classical Navier-Stokes and continuity equations for incompressible fluids

$$\rho \frac{\partial \boldsymbol{u}}{\partial t} + \rho \boldsymbol{u}.\nabla \boldsymbol{u} = -\nabla \mathrm{P} + (\mu_l^* + \mu_t)\nabla^2 \boldsymbol{u} + \boldsymbol{F}_{em} + \boldsymbol{F}_b \tag{3.22}$$

$$\boldsymbol{\nabla}.\boldsymbol{u} = 0 \tag{3.23}$$

where **u** is the velocity vector, P is the pressure, μ_l^* is the effective laminar viscosity, and $\mathbf{F}_{em}$ and $\mathbf{F}_b$ representing the Lorentz and buoyancy body forces, respectively. The effective viscosity may be given through the turbulent and laminar components. The turbulent viscosity component is given by the k-ε model, which will be discussed in further detail in a later subsection.

To describe fluid flow in the two-phase mushy zone, the velocity vector is defined through the weighted contribution of the solid and liquid phases with respect to solid fraction.

$$\boldsymbol{u} = \boldsymbol{u}_s f_s + \boldsymbol{u}_l (1 - f_s) \tag{3.24}$$

The physical properties are described in a similar manner as Equation (3.24). The subscripts s and l represent the solid and liquid phases, respectively.

The flow in the suspended particle region is described by the homogeneous two-phase flow model. In this model, the solid crystallites and the liquid are considered to have nearly equal density, and thus are aggregated into a pseudofluid. This allows for the time-averaged velocities of the solid and liquid phases to be assumed equal ($\bar{\mathbf{u}}_\mathbf{l} \equiv \bar{\mathbf{u}}_\mathbf{s}$). The conservation equations for the time-averaged velocity of the pseudofluid are similar in form to the Navier-Stokes equation given in Equation (3.22).

$$\rho \frac{\partial \boldsymbol{u}}{\partial t} + \rho \boldsymbol{u}.\nabla \boldsymbol{u} = -\nabla P + (\mu_l^* + \mu_t)\nabla^2 \boldsymbol{u} + \boldsymbol{F}_{em} + \boldsymbol{F}_b + \boldsymbol{F}_d \tag{3.25}$$

The continuity equation for the suspended particle region is identical to Equation (3.23). The additional term, $\mathbf{F}_d$, is a body force that damps the flow due to the presence of the solid phase, and will be described later in further detail.

In the fixed particle region, defined by $f_c<f_s<1$ (where f_c represents the coherency solid fraction), the solid crystallites are interlocked among each other. Therefore, the velocity of the solid is held to be identically zero ($\mathbf{u}_s=0$), giving $\mathbf{u}_l=\mathbf{u}/f_l$. Furthermore, the solid network prevents the application of Lorentz forces within the liquid phase, making $\mathbf{F_{em}}$ equal to zero. The modified Navier-Stokes equation is given by

$$\rho\frac{\partial \boldsymbol{u}}{\partial t}+\frac{\rho}{f_l}\boldsymbol{u}.\nabla\boldsymbol{u}=-\nabla P+\mu_l^*\nabla^2\boldsymbol{u}+\boldsymbol{F}_b+\boldsymbol{F}_d \tag{3.26}$$

As with the other two flow regions, the continuity equation is again given by Equation (3.22). Note that the turbulent viscosity term no longer appears behind the vector Laplacian as it is assumed that turbulence is completely damped in the interdendritic channels. This assumption is reasonable since the spacing between crystallite arms is less than or equal to the Taylor mixing length used in the k-ε models.

3.4.2 Description of Source Terms in the Conservation Equations

To describe the buoyancy force, $\mathbf{F}_b$, over the three flow regions in terms of temperature, the linear Boussinesq approximation is used

$$\boldsymbol{F}_b=\rho_0[1-\beta(T-T_0)]\boldsymbol{g} \tag{3.27}$$

where β is the volume coefficient of thermal expansion. The naught terms in Equation (3.27), ρ_0 and T_0, represent the reference density and temperature, respectively; in this work, the values are given as those of the bulk liquid.

The expression for the damping force, $\mathbf{F}_d$, is dependent on the flow region in question, with the extent of damping dependent on the solid fraction. In the suspended particle region, the

damping is due to the crystallite interactions with the turbulent eddies, while in the fixed particle region the damping is given by the pressure drop due to Darcy's law. These are represented below in Equation (3.28).

$$\boldsymbol{F_d} = \begin{cases} \frac{-2\rho\sqrt{6k}I_T f_s^{1-n} f_c^n}{D_g}\boldsymbol{u} & \forall f_s \in (0, f_c) \\ -\frac{\mu_l^*}{K}\boldsymbol{u} & \forall f_s \in [f_c, 1] \end{cases} \tag{3.28}$$

In the expression for the suspended particle domain, k represents the turbulent kinetic energy, I_T is the turbulent intensity, D_g is the grain size, and n is a grain growth exponent ranging from zero to one dependent on the crystallite growth kinetics. In the fixed particle region, K represents the permeability of the interdendritic medium, and is given by the well-known Carman-Kozeny equation. A derivation of the damping force in the suspended particle region resulting from turbulent interactions is given in subsection 3.4.4.

The effective laminar viscosity is also dependent on the behavior of the solid crystallites in each flow domain. In the bulk liquid and fixed particle regions, the viscosity is given by the molecular value only; in the suspended particle region, however, the particles serve to induce rheological behavior in the pseudofluid, which is given by the Mooney equation [127]. The expression for the effective laminar viscosity over all values of solid fraction is given by

$$\mu_l^* = \begin{cases} \mu_0^* & f_s \equiv 0 \\ \mu_0^* exp\left[\frac{2.5 f_s}{1-{f_s}/{0.68}}\right] & \forall f_s \in (0, f_c) \\ \mu_0^* & \forall f_s \in (f_c, 1) \end{cases} \tag{3.29}$$

where μ_0^* in the above equation is the molecular viscosity of the material

3.4.3 Low-Re Turbulence Model for Homogeneous Flow

For single-phase flows in domains consisting of fixed boundaries, the turbulent characteristics of the flow are described using the k-ε model developed by Launder and Spalding

[126], along with appropriate representations of the viscous sublayer near the walls. In a two-phase region where one of the phases is solid and assumed undeformable, the Launder-Spalding model cannot accurately describe the effects regarding the presence of the solid phase on the turbulent field using the traditional wall functions. Instead, the turbulent characteristics are described by a k-ε model adapted for low-Re flows by Jones and Launder [120]. Assuming isotropic turbulent behavior, the equations for the turbulent kinetic energy and turbulent energy dissipation are given by

$$\rho\frac{\partial k}{\partial t}+\rho(\boldsymbol{u}.\nabla)k=\nabla.\left(\frac{\mu_t}{\sigma_k}\nabla k\right)+G-\rho\varepsilon \tag{3.30}$$

$$\rho\frac{\partial \varepsilon}{\partial t}+\rho(\boldsymbol{u}.\nabla)\varepsilon=\nabla.\left(\frac{\mu_t}{\sigma_\varepsilon}\nabla \varepsilon\right)+C_1\frac{\varepsilon}{k}G-C_2\frac{\varepsilon^2}{k} \tag{3.31}$$

In these equations, C_1 and C_2 are functions dependent on the intensity of the flow. G represents the turbulent shear generation term, and is written below in abbreviated tensor form.

$$G_{ij}=\mu_t\left(\frac{\partial u_i}{\partial x_j}+\frac{\partial u_j}{\partial x_i}\right)\frac{\partial u_i}{\partial x_j} \tag{3.32}$$

Given the values of the turbulent kinetic energy and the turbulent energy dissipation rate, the turbulent viscosity is given by

$$\mu_t=C_\mu\rho k^2/\varepsilon \tag{3.34}$$

C_μ is defined as the drag coefficient and, like C_1 and C_2, has a functional dependence with respect to the flow intensity

In describing the functions for C_1, C_2, and C_μ, necessary to ensure closure of the turbulence problem, the flow intensity is conveniently described as a ratio of the turbulent viscosity to the molecular viscosity of the bulk liquid, referred to as the turbulent Reynolds number, $R_T=\rho k^2/\mu_l{}^*\varepsilon$. The functions by are given by Jones and Launder [120] as

$$C_1 = 1.44 \tag{3.36}$$

$$C_2 = 1.92\left(1 - 0.3exp(-R_T^2)\right) \tag{3.37}$$

$$C_\mu = 0.09exp\left[\frac{-3.4}{1+\frac{R_T}{50}}\right] \tag{3.38}$$

It is important to note that at high values of R_T, the functions are equal to the prefactors in each equation

3.4.4 Determination of the Damping Force

To determine the damping force in the suspended particle region (from Equation (3.28)), consider a volume element containing N particles and occupying a total volume V. Consistent with the homogeneous flow model, let the time-averaged velocities of each phase in the volume element be identically equal to one another ($\bar{\mathbf{u}}_\mathbf{l} \equiv \bar{\mathbf{u}}_\mathbf{s}$). Furthermore, assume that the turbulent fluctuations be confined to the liquid only (i.e. $\mathbf{u'}_\mathbf{s} \equiv 0$). For this to be valid, the volumetric drag force $\mathbf{F_d}$ must be equal to the sum of the Reynolds stresses at the particle surface; that is

$$\iiint_V \boldsymbol{F_d} dV = \oiint_{A_p} \bar{\boldsymbol{\tau}}_\boldsymbol{t} . \tilde{\boldsymbol{n}} dS \tag{3.37}$$

where $\tilde{\mathbf{n}}$ is the unit normal to the cross-section of the flow. The time-averaged Reynolds stress is given in tensor form as

$$\bar{\boldsymbol{\tau}}_\boldsymbol{t} = -\rho\overline{u'_\imath u'_\jmath} \tag{3.38}$$

Assuming isotropic turbulence, this equation may be rewritten in terms of the turbulent kinetic energy, k, and the unit tensor, **I** [121].

$$\bar{\boldsymbol{\tau}}_\boldsymbol{t} = -\frac{2}{3}\rho k \boldsymbol{I} \tag{3.39}$$

Therefore

$$\boldsymbol{F}_d V = \oiint_{A_p} \bar{\boldsymbol{\tau}}_\boldsymbol{t} . \tilde{\boldsymbol{n}}\, dS = -\frac{2}{3}\rho k A_p \frac{\boldsymbol{u}}{|\boldsymbol{u}|} \tag{3.40}$$

Let A_p be the sum of the surface areas of all the particles in the control volume. For uniform particle size with respect to solid fraction, $A_p=\pi d_g^2 N$. The number of particles in the control volume is given by

$$N = \frac{total\ mass\ of\ the\ solid}{mass\ of\ one\ particle} = \frac{6 f_s V}{\pi d_g^3} \tag{3.41}$$

where d_g is the particle diameter of the equivalent sphere, and is a function of solid fraction. This gives

$$A_p = \frac{6 f_s V}{d_g} \tag{3.42}$$

Inserting this relation into (3.40) gives

$$\boldsymbol{F}_d = -\frac{4\rho k f_s}{d_g |\boldsymbol{u}|}\boldsymbol{u} \tag{3.43}$$

The turbulent intensity, I_T, is defined by

$$I_T = \sqrt{\frac{2k}{3}}|\boldsymbol{u}|^{-1} \tag{3.44}$$

The force is then rewritten as

$$\boldsymbol{F_d} = -\frac{2\sqrt{6}\rho\sqrt{k} I_T f_s}{d_g}\boldsymbol{u} \tag{3.45}$$

Let d_g is defined in terms of a power law

$$d_g = A_0 f_s^{\,n} + B_0 \tag{3.46}$$

where A_0 and B_0 are grain growth constants. For $d_g = 0$ at $f_s = 0$ and $d_g = D$ at $f_s = f_c$, where D is the final grain size and f_c is the coherency solid fraction, (3.46) becomes

$$d_g = D_g (f_s/f_c)^n \tag{3.47}$$

This gives the final form of the damping force per unit volume used in Equation (3.xx).

$$\boldsymbol{F_d} = -\frac{2\sqrt{6}\rho\sqrt{k} I_T f_s^{1-n} f_c^n}{D_g}\boldsymbol{u} \tag{3.48}$$

3.5 Numerical Solution of the Transport Equations

To solve the governing equations, for the transport quantities, the control volume method was used. In the control volume method, the metal domain is subdivided into a number of cells bounded by constant values of r and z called *control volumes*. In each control volume, the value of the transport quantity is presumed to dominate over the entire cell.

Since the conservation equations all follow a similar template, the canonical form of the conservation equation for general variable ϕ is given by

$$\rho \frac{\partial \phi}{\partial t} + \rho \boldsymbol{u}.\nabla \phi = \nabla.(\Gamma_\phi \nabla \phi) + S_\phi \tag{3.49}$$

where Γ_ϕ and S_ϕ are the variable-dependent diffusion coefficient and source terms.

To account for the coupling between the pressure and the velocity, a staggered-grid approach is used. An illustration of this grid structure is shown in Figure 3.3, and sample sketches of scalar and vector cells are shown in Figures 3.4 and 3.5, respectively. Returning to Fig 3.3, it can be seen that the control volumes for the vector quantities (u,v) are offset for those of the scalar quantities (T, k, ε, etc.)

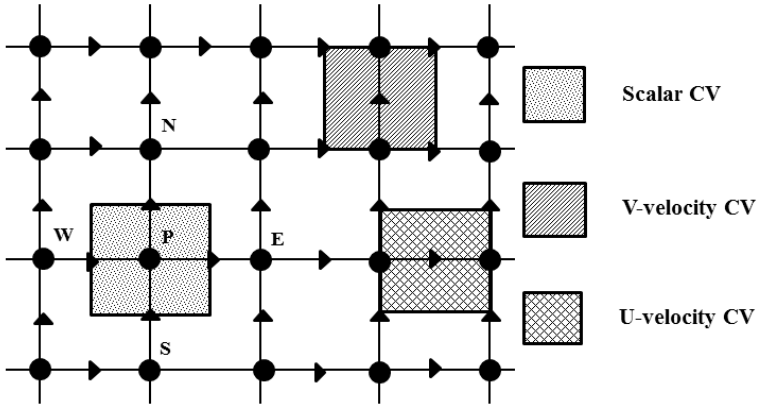

Figure 3.3. Sketch of the control volumes

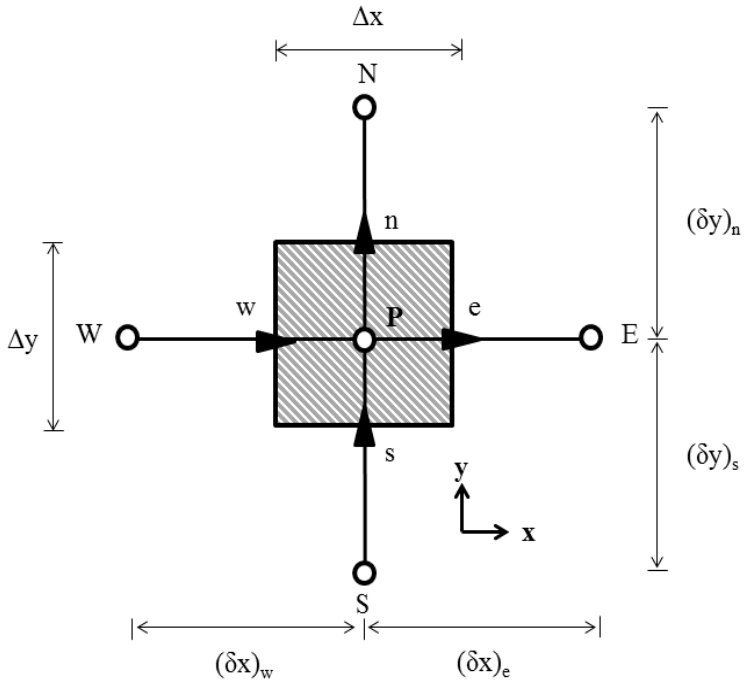

Figure 3.4. Sketch of a scalar control volume

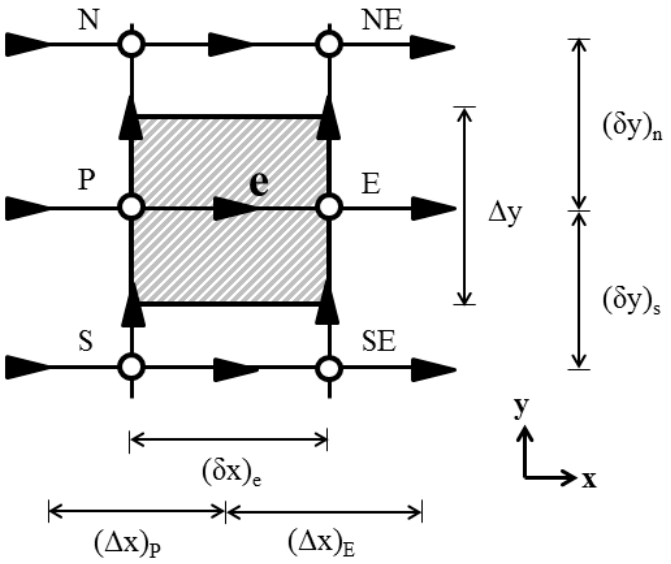

Figure 3.5. Sketch of a vector control volume

Upon integrating over the appropriate control volume, using the scalar cell as an example, the value of each variable at point P, ϕ_P, may be put in terms of the surrounding points (N, S, E, and W):

$$a_P\phi_P = a_N\phi_N + a_S\phi_S + a_E\phi_E + a_W\phi_W + Su \tag{3.50a}$$

$$a_P = a_W + a_E + a_N + a_S - Sp \tag{3.50b}$$

where a_i represents the coefficients originating from the convective and diffusive terms in Equation (3.38). Su and Sp correspond to source terms; the Sp term is linearized with respect to ϕ_p.

To evaluate the coefficients, it is convenient to write them in terms of convective fluxes, F_i, and diffusive conductances, D_i. Using the scalar control volume as an example, taking the volume integral and using Green's theorem for the convective term yields

$$\rho \iiint_{vol} \boldsymbol{u}.\nabla\phi \, dV = \rho \oiint (\boldsymbol{u}.\hat{\boldsymbol{n}})\phi \, dS = (\rho u\phi)_e \Delta r - (\rho u\phi)_w \Delta r + (\rho v\phi)_n \Delta z - (\rho v\phi)_s \Delta z \tag{3.51}$$

The convective fluxes are

$$F_E = (\rho u)_e \Delta z; \quad F_W = (\rho u)_w \Delta z; \quad F_N = (\rho v)_n \Delta r; \quad F_S = (\rho v)_s \Delta r \tag{3.52}$$

The same can be done for the conductances

$$D_E = \frac{\Gamma_e \Delta r}{\Delta z}; \quad D_W = \frac{\Gamma_w \Delta r}{\Delta z}; \quad D_N = \frac{\Gamma_n \Delta z}{\Delta r}; \quad D_S = \frac{\Gamma_s \Delta z}{\Delta r} \tag{3.53}$$

Using these definitions and employing the well-known "upwind scheme," the coefficients are defined as

$$a_E = D_E + [\![-F_E, 0]\!] \tag{3.54a}$$

$$a_W = D_W + [\![F_W, 0]\!] \tag{3.54b}$$

$$a_N = D_N + [\![-F_N, 0]\!] \tag{3.54c}$$

$$a_S = D_S + [\![F_S, 0]\!] \tag{3.54d}$$

where [A,B] denotes the greater of A and B.

The accumulation term in Equation (3.37) may be discretized as follows:

$$\rho \iiint_{vol} \frac{\partial \phi}{\partial t}\, dV = \frac{\rho(\phi_P - \phi_P^*)}{\Delta t} \Delta V \tag{3.55}$$

where ϕ_p^* is the value of the variable at the previous time step. Since one term is linearized and the other is not, the accumulation term may be split among Su and Sp as follows:

$$Su = \rho \phi_P^* \Delta t^{-1} \Delta V; \quad Sp = -\rho \Delta t^{-1} \Delta V \tag{3.56}$$

Pertaining to the integrated form of S_ϕ, the term may also be divided among the Su and Sp terms in such a way that ensures the stability of the matrix solver. For a more in-depth discussion, see Reference [54].

CHAPTER 4

RESULTS AND DISCUSSION

The model developed in Chapter 3 for describing the temperature and flow phenomena in an electromagnetically stirred melt during solidification was used to investigate unidirectional solidification of alloys in a bottom chill mold subjected to an axial magnetic field. This study examines the variation of the velocity and turbulent characteristics, in both the bulk liquid and mushy zone, with respect to solidification morphology. Emphasis will be placed on the influence of grain size and solidification rate on the flow in the mushy region.

4.1 Description of the Model System

Figure 4.1 shows a sketch of the bottom chill mold used in this study. The mold consists of an insulating refractory tube and a water-cooled stainless steel chill block. The chill block allows water to flow through a cavity close to the top surface of the chill block, allowing for a constant and uniform heat transfer coefficient at the chill block/metal interface. In this study, the melt stirring is provided by a three-turn induction coil situated at one-half of the ingot height.

Due to the axial symmetry of the system, the electromagnetic field, fluid flow, and heat transfer problems are two-dimensional, and the field equations need only to be calculated in the r-z plane. The solution domain for the temperature, velocity, and turbulent fields consists of the metal only, and is divided into a 30x30 non-uniform grid, shown in Figure 4.2. The boundary conditions are also shown in this figure. For the electromagnetic field calculations, the solution

domain includes both the metal and the stainless steel chill block. In order to accurately describe the exponential decay of the magnetic field in the metal due to the skin effect, a finer grid is used near the outer radius.

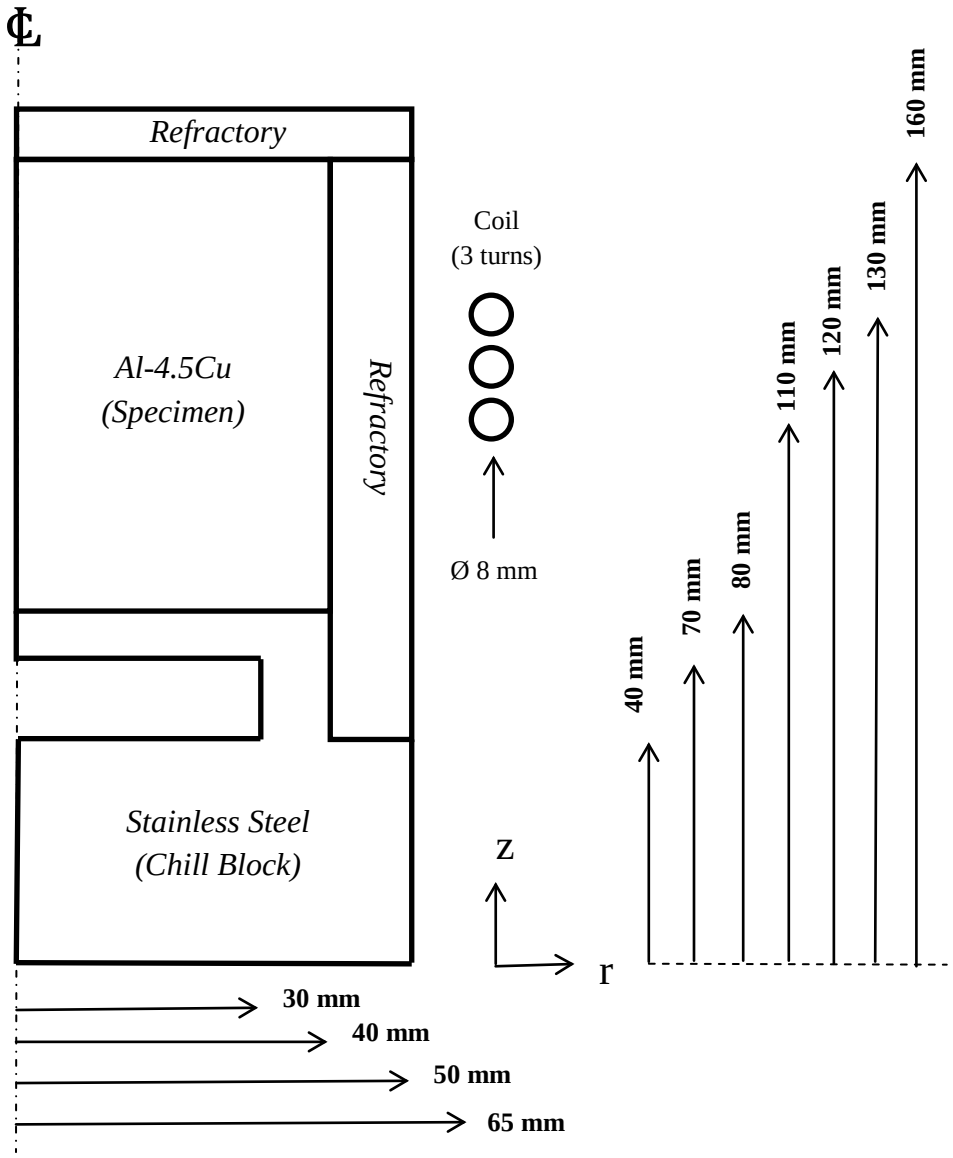

Figure 4.1 Detailed Sketch of the Modeled System.

$$\frac{\partial T}{\partial n} = 0, u = 0$$
$$\frac{\partial v}{\partial n} = 0, \frac{\partial k}{\partial n} = 0, \frac{\partial \varepsilon}{\partial n} = 0$$

$$\frac{\partial T}{\partial n} = 0, \frac{\partial u}{\partial n} = 0$$
$$v = 0, \frac{\partial k}{\partial n} = 0, \frac{\partial \varepsilon}{\partial n} = 0$$

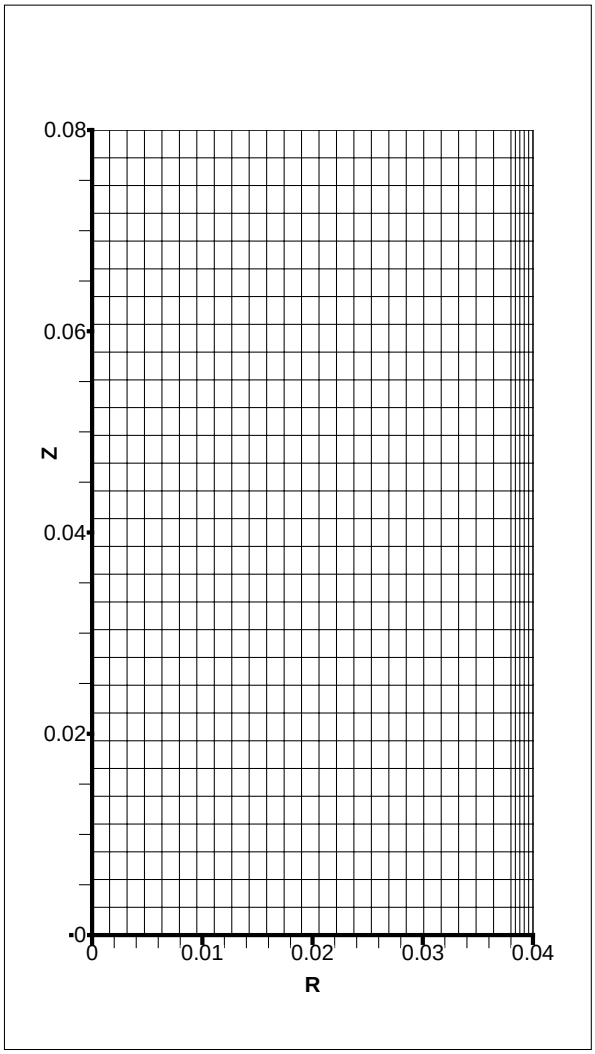

$$\frac{\partial T}{\partial n} = 0, u = 0$$
$$v = 0, k = 0, \frac{\partial \varepsilon}{\partial n} = 0$$

$$q = h(T - T_\infty), \quad u = 0$$
$$v = 0, \quad k = 0, \quad \frac{\partial \varepsilon}{\partial n} = 0$$

Figure 4.2 Gridded solution domain with boundary conditions

Calculations were carried out for solidification of Al-4.5%Cu with an initial temperature of 670°C. The thermophysical properties are shown in Table 4.1. The coil current and frequency used in this study were 200 A and 500 Hz, respectively. The fluid flow phenomena in the mushy zone were investigated for the globular and dendritic solidification morphologies. A coherency value of 0.25 was used to represent the dendritic morphology, while a value of 0.5 was assigned to the globular morphology. In order to determine the effect of the final grain size of the cast alloy on the damping of the flow in the mushy zone, three grain sizes were studied—namely 100 μm, 200 μm, and 500 μm—for each morphology. The effect of the heat extraction rate on solidification of the alloy was investigated by varying the heat transfer coefficient in the range of 250-750 W/m^2-K.

Thermophysical Properties for Al-4.5%Cu	
Solid density:	2979 kg/m^3
Liquid density:	2979 kg/m^3
Solid thermal conductivity:	188.3 W/m-K
Liquid thermal conductivity:	192.5 W/m-K
Solid heat capacity:	870.5 J/kg-K
Liquid heat capacity:	1059 J/kg-K
Electrical conductivity:	$1.28*10^6$ Mho/m
Liquidus temperature:	648°C
Solidus temperature:	564°C
Latent heat of fusion:	389000 J/kg
Molecular viscosity:	0.0015 Pa-s

Table 4.1 Thermophysical properties used in the calculations.

4.2 Electromagnetic Field

Figure 4.3 shows the computed electromagnetic (Lorentz) force field for a coil current of 200A and a frequency of 500 Hz. As expected, the forces exhibit positive divergence with respect to the middle section of the ingot, which is expected since this point is coincident with the axial midpoint of the coil. The maximum value of the Lorentz forces lies at the previously mentioned point, with a magnitude of 10^4 N/m^3, and the magnitude of the force expresses a marked decrease along any given constant z plane as r tends less than R.

Of particular interest is the rotational component of the force, given by rot($\mathbf{F}_{em}$), which drives the flow. This is shown in Figure 4.4. Upon inspection, one will easily notice that the highest degrees of rotation occur at the outer radius at z=0.02 m and z=0.06 m, with opposite signs, and that the curl of the field is zero at z=0.04 m. This means that the flow will feature two axisymmetric recirculating loops, with the bottom loop rotating counterclockwise and the upper loop rotating clockwise. The influence of the magnetic shields can also be seen in this figure. It is observed that the magnitude of the curl is larger for z < 0.04 m. This is a result of the stronger coupling of the magnetic field with the chill block relative to the metal, as the electrical conductivity is higher for stainless steel than Al-4.5%Cu.

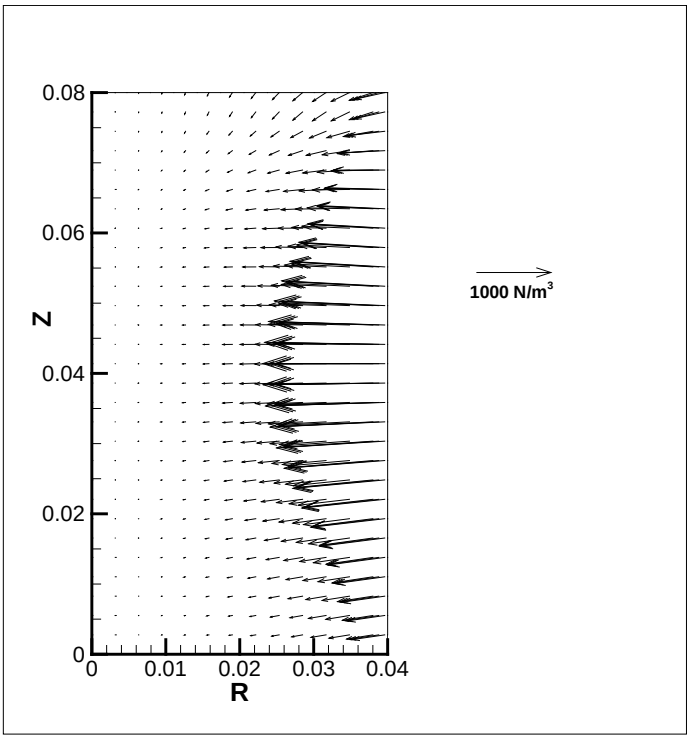

Figure 4.3 Lorentz force distribution in the metal.

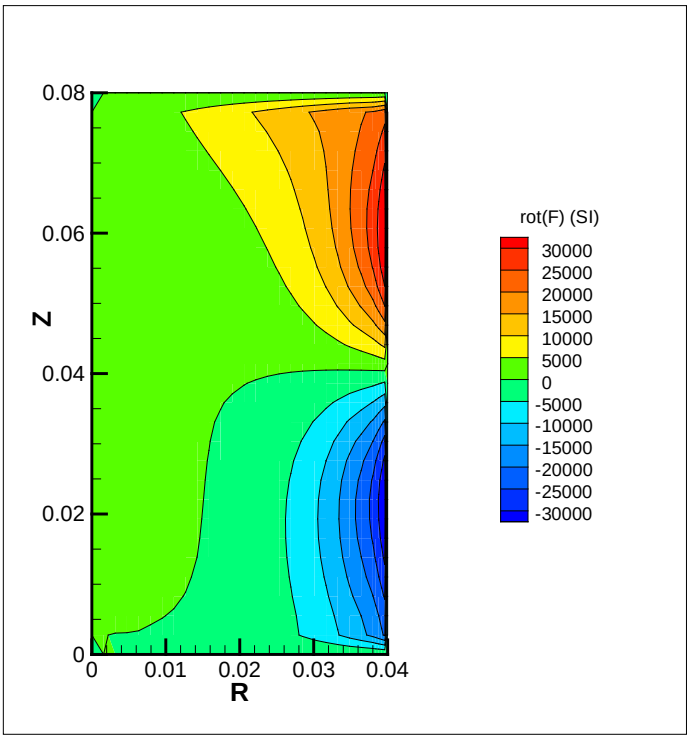

Figure 4.4 Curl of the EM Forces (units are in SI)

Figure 4.5 shows the electrical energy dissipation in the metal. Like the electromagnetic forces, the maximum values of Joule heating occur at the axial midpoint near the induction coil. The maximum value of Joule heating was around 10^5 W/m^3, and decreases for greater distance from the field source. For the case investigated, the total heat generated in the metal was 13.5 W. This quantity is much smaller than the rate of latent heat extraction from the melt, and therefore the effect of Joule heating on the overall solidification rate is negligibly small. However, since Joule heating acts to reduce the solidification rate, there will be some localized effect in regions where Joule heating is relatively high (i.e. nearest the field source).

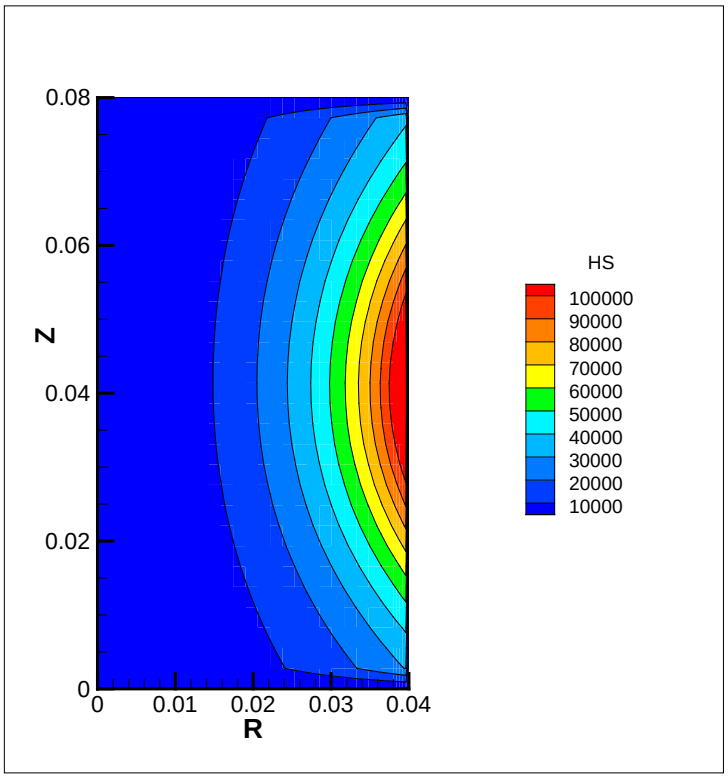

Figure 4.5 Joule heating in the metal (units are in SI)

4.3 Computed Results for Globular Solidification Morphology

4.3.1 Fluid Flow and Temperature Fields

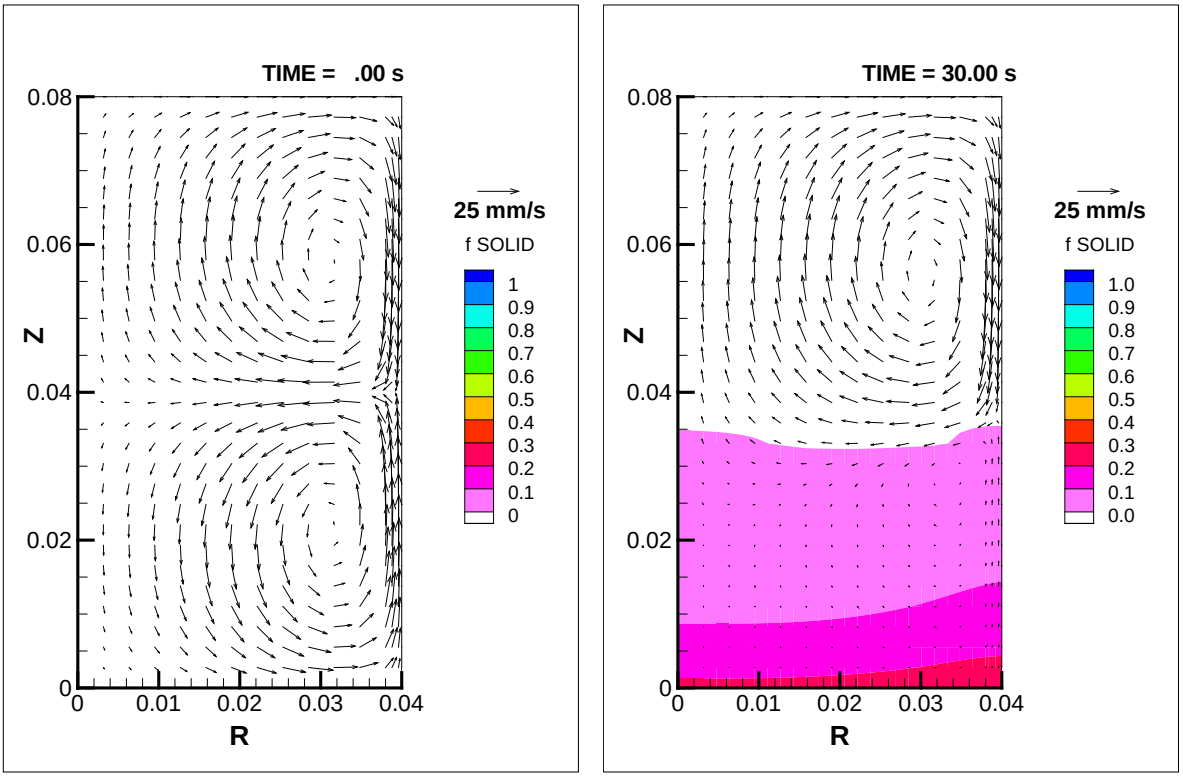

(a) (b)

Figure 4.6 Velocity and temperature fields for (a) t=0; (b) t=30 s

Figures 4.6 and 4.7 show a typical evolution of the velocity and temperature fields—presented in terms of solid fraction—during solidification for a grain size of 200 μm and heat transfer coefficient of 500 W/m^2-K. Figure 4.6a shows the velocity field prior to solidification (t=0). As seen in this figure, the velocity field is characterized by two axisymmetric, recirculating loops, which is expected for a stationary magnetic field. These two loops are approximately the same size due to the positioning of the coil at the axial midpoint of the specimen. It can also be seen that the characteristic velocity is approximately 20 mm/s. After 30s (Figure 4.6b) the temperature at the base of the specimen has dropped below the liquidus

temperature, and the mushy zone now comprises approximately half of the height, causing significant changes in the flow intensity in that region. However, it is clearly seen that the maximum value of f_s is less than the coherency value, f_c, of 0.5. The solid fraction contours are shown to align themselves tangentially with respect to the direction of the flow. This means that convection is the dominant mode of heat transfer. It should also be observed that while the magnitude of the velocity in the upper recirculating loop remains approximately the same as its initial value, the velocity in the lower recirculating loop is sharply reduced by an order of magnitude. This is a result of the damping force acting on the flow, the magnitude of which increases with increasing solid fraction.

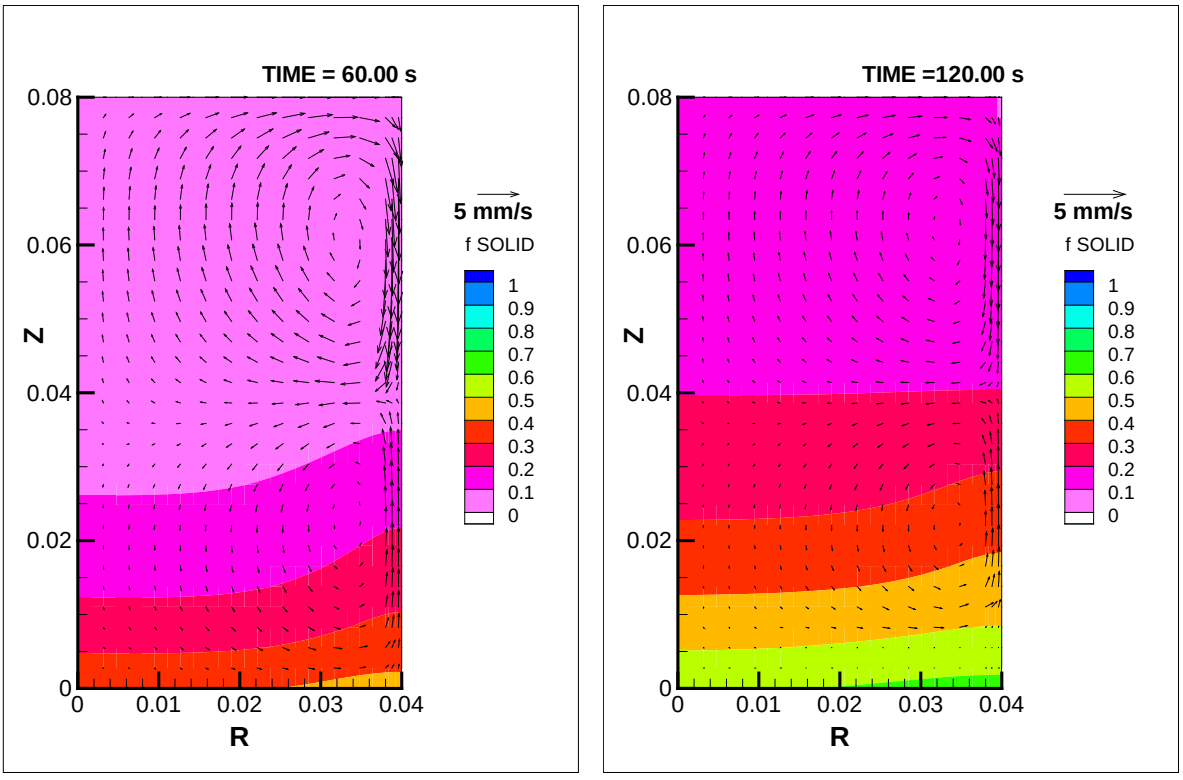

(a) (b)

Figure 4.7 Velocity and temperature fields for (a)t=60; (b) t=120 s

Figure 4.7a shows the velocity and temperature fields after 60 seconds. At this solidification time, the mushy zone now covers the entire domain, and the maximum value of solid fraction is less than the coherency, meaning that solidification is still in the suspended particle region. Note the change of the velocity scale for easier viewing. As seen in this figure, the characteristic velocity in the upper loop is approximately 5 mm/s, and drops to less than 1 mm/s at the base of the metal, where solid fraction is close to coherency. These values are an order of magnitude smaller than the velocity in the bulk liquid.

The flow in the fixed particle region is first shown in Figure 4.7b. This figure corresponds to a solidification time of 120 seconds. As seen in this figure, the transition from the suspended particle region to the fixed particle region is characterized by another significant drop in the velocity. This is expected, as the formation of a stationary dendrite network provides additional resistance to liquid phase motion via a reduction of the permeability in Darcian flow. The significance of the decrease of the velocity is also observed in this figure. It can be seen that the curvature of the isotherms at the mold wall decreases along with the velocity at higher solid fraction, and the isosurface normal begins to align itself parallel to the heat flux. Thus it is clear that the coherency point also marks the transition between convection-dominant heat transfer to diffusion-dominant transfer.

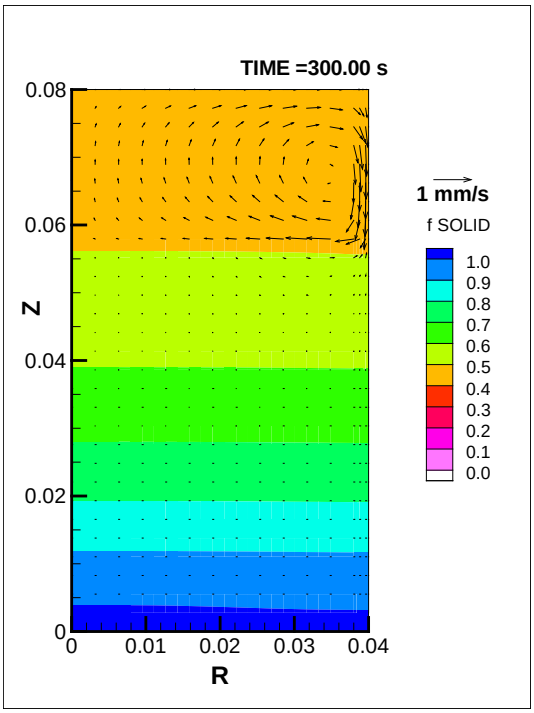

(a)

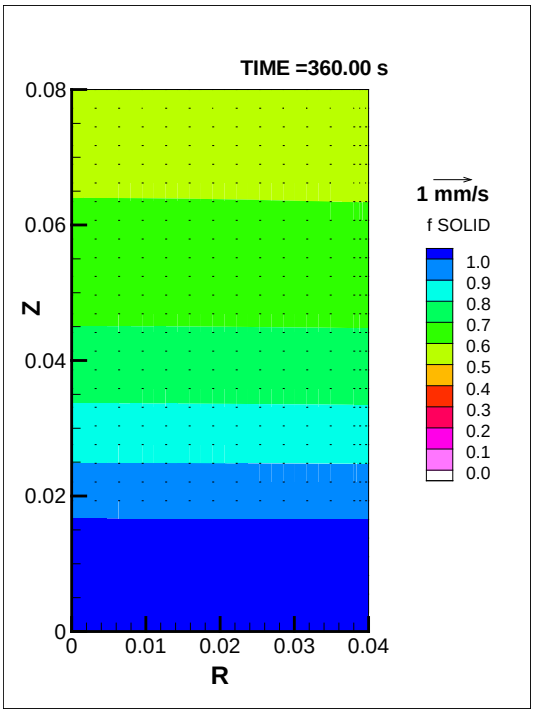

(b)

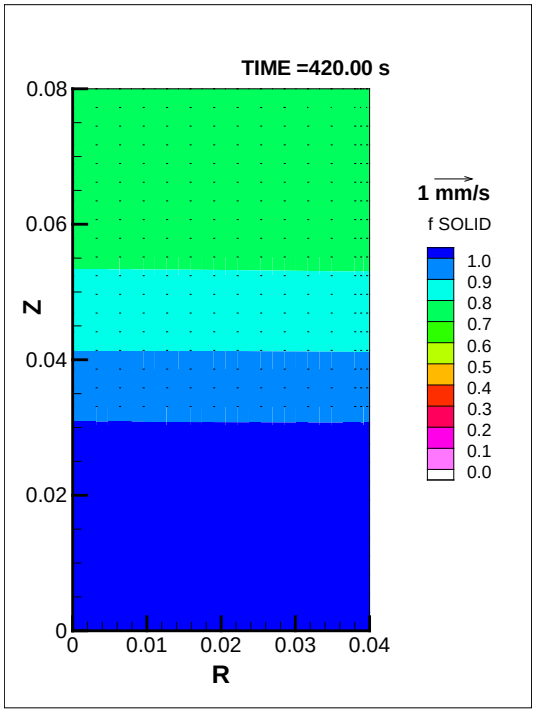

(c)

Figure 4.8 Velocity and temperature fields at later stages of solidification

Figures 4.8(a-c) show the evolution of velocity and temperature fields at later stages of solidification corresponding to 300, 360, and 420 seconds, respectively, where the solid fraction is above the coherency value (fixed particle region). At t=300s, most of the metal is in the fixed particle region, with only the top of the ingot remaining in the suspended particle region. It is clear that heat transfer occurs via conduction. Observe that the flow only penetrates a few millimeters into the fixed particle region, as the influence of Darcy damping is substantially stronger than momentum transfer at the interface, in addition to the body forces being nil for $f_s < f_c$. After 360 seconds, the fixed particle region now covers the entire domain. The velocity in this region is now nil due to Darcy damping and the lack of any body forces to drive the flow in the fixed particle region. Such is also the case for t=420s as well, where no fluid flow occurs and heat transfer is by conduction only. This occurs until the end of solidification after 492 seconds.

Figure 4.9 presents a typical evolution of the turbulent kinetic energy for globular solidification with grain size of 200 μm and a heat transfer coefficient of 500 W/m^2-K. The turbulence level in the bulk liquid is shown in Figure 4.9a. As seen in this figure, the turbulent kinetic energy varies on the order of 10^{-3} J/kg near the centerline to 10^{-4} J/kg near the mold wall. When compared to the fluid velocity, this suggests that the flow is highly turbulent in the bulk liquid. In the initial stages of solidification, the turbulence level becomes highly attenuated in the mushy region, as shown in Figure 4.9b. After 60s, it was found that turbulence was completely dissipated.

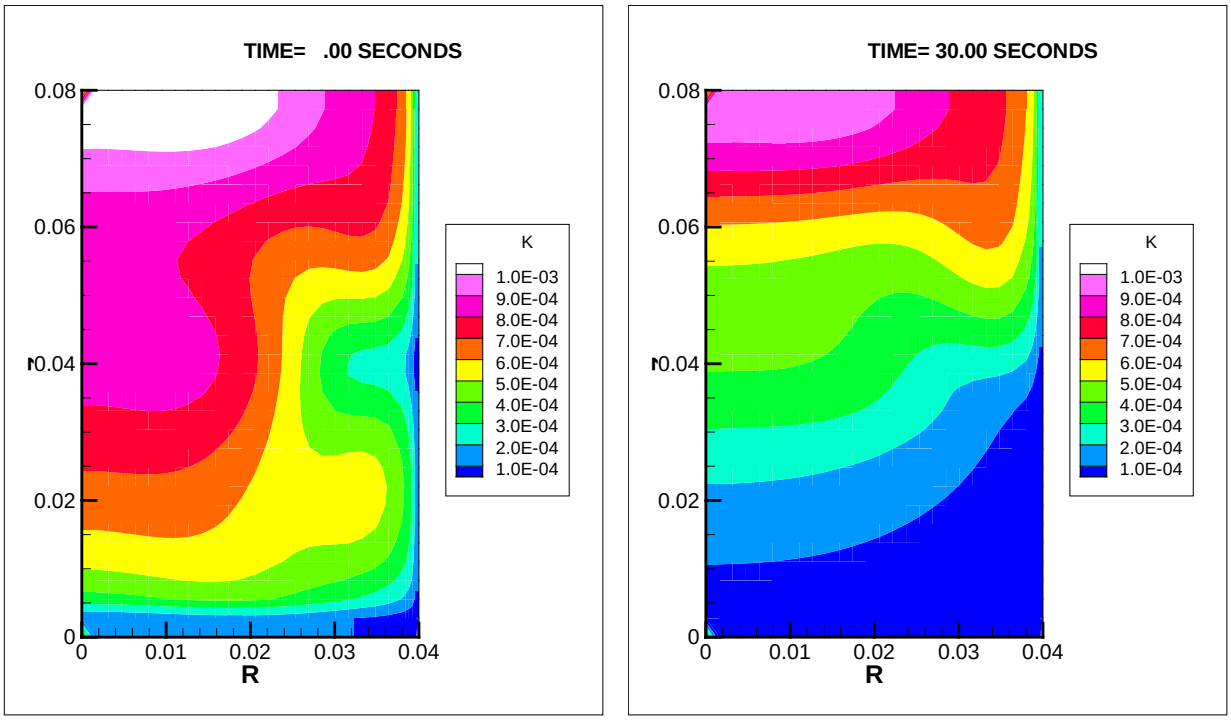

(a) (b)

Figure 4.9 Turbulent kinetic energy profiles for (a) t=0s; (b) t=30s

4.3.2. Effect of Solidification Parameters

Figure 4.10 shows cooling curves for three different heat transfer coefficients investigated, each taken at z/H=0.8 for a grain size of 200 μm. As seen in this figure, the solidification times, defined by the time difference between the intersection of the cooling with the solidus and liquidus lines, were determined to be 917, 453, and 301 seconds for heat transfer coefficient values of 250, 500, and 750 W/m^2-K, respectively. As expected, the solidification time increases for decreasing h, reflecting the reduced heat extraction rate. There are three points of inflection in each cooling curve. Starting from t=0, the first and last points of inflection are at the liquidus and solidus temperatures, respectively. These correspond to the beginning and end of latent heat evolution. The second point of inflection at the coherency is of particular interest,

and corresponds to the previously mentioned transition in heat transfer modes from convection- to diffusion-dominant.

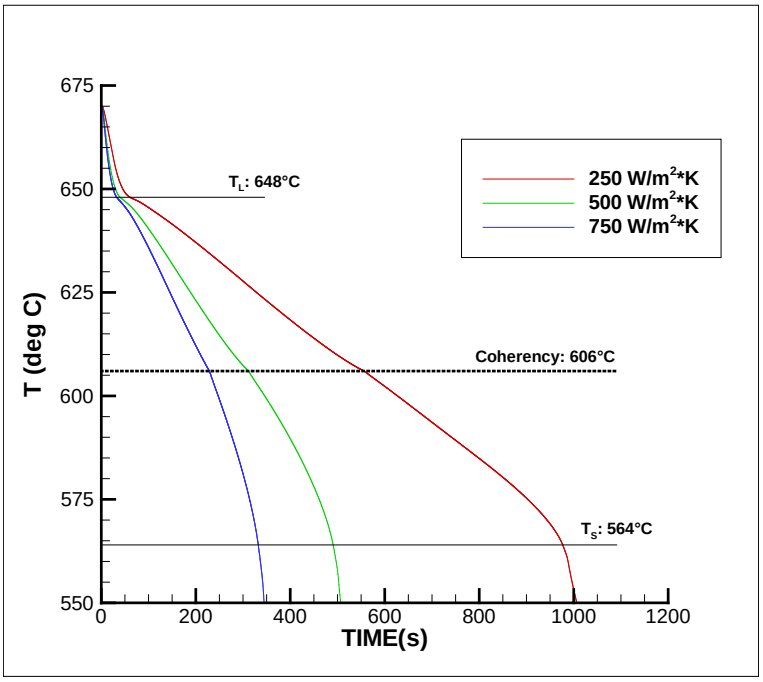

Figure 4.10 Cooling curves for globular solidification at various h

Figure 4.11 gives the centerline velocity for z/H = 0.8 as a function of solid fraction for three different grain sizes and a heat transfer coefficient of 500 W/m^2-K. As seen in this figure, there is a sharp decrease in the flow intensity in the initial stage of solidification ($0<f_s<0.1$) where the flow is damped by turbulent decay. This is expected, as damping is strongest in the region of solid fraction $0<f_s<0.05$, where the particles are smallest and thus have the highest surface-to-volume ratio. It is also seen that the intensity of the flow is stronger for increasing final grain size. This stems from a smaller particle number density, which decreases the amount of surface area where the Reynolds stresses can act. In terms of heat transfer, this means that higher cooling rates for large-grained structures at the beginning of solidification.

As the solid fraction increases beyond a solid fraction of 0.1, the velocity remains nearly constant, meaning very small changes in the rate of convective transfer. At f_s~0.4, the flow intensity decreases again until becoming almost negligible at the coherency point. Damping in this region occurs due to a drop in the pressure gradient near the D'Arcy interface. The additional damping also reduces the rate of heat transfer by convection to almost nil. As a result, heat transfer for $f_s > 0.4$ is primarily driven by conduction.

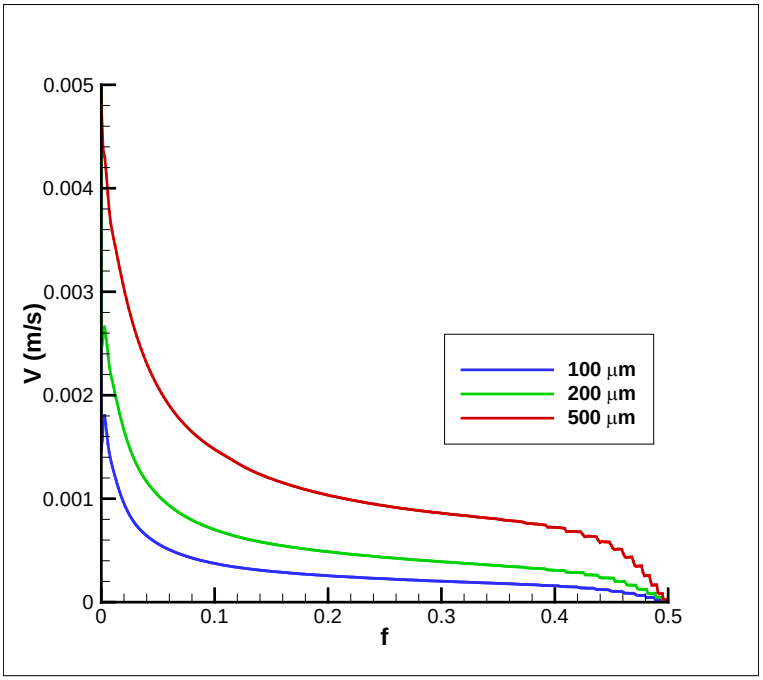

Figure 4.11 Velocity as a function of solid fraction for various D_g

Figure 4.12 shows a cooling curves for grain sizes of 100, 200, and 500 μm, with the heat transfer coefficient of 500 W/m^2-K. It can be clearly seen that the cooling rates for the fixed particle region and the bulk liquid are nearly the same, but deviate within the suspended particle region. Further inspection shows that the cooling rate is slightly higher for larger grain size. This is consistent with the results shown in Figure 4.11, where the velocity was highest for large grains and by corollary had the largest convective heat flux.

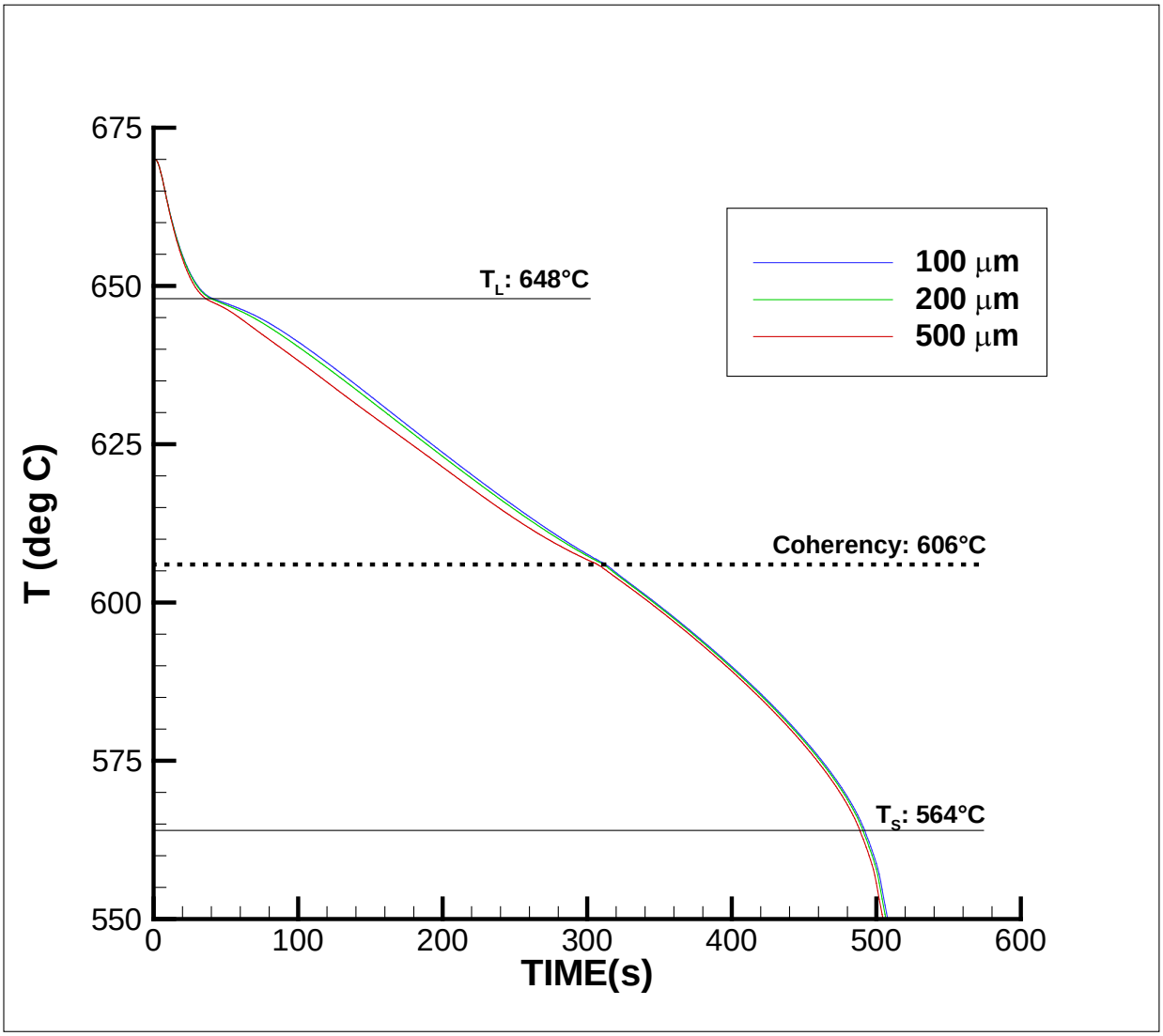

Figure 4.12 Cooling curves for globular solidification for various D_g

4.4 Computed Results for Dendritic Solidification Morphology

4.4.1 Fluid Flow and Temperature Profiles

Figure 4.13 shows the evolution of the velocity and temperature fields—the latter of shown in terms of solid fraction—during solidification for a gain size of 200 μm and heat transfer coefficient of 500 W/m^2-K. As seen in Figure 4.13a, the velocity field prior to solidification is identical to that of globular solidification in Figure 4.6a, which is expected. After 30 seconds, displayed in Figure 4.13b, the suspended particle region essentially covers the entire bottom half of the ingot, similar to that of globular solidification, with the velocity being damped by an order of magnitude. It should be said here that the magnitude of the velocity in the suspended particle region is higher for dendritic solidification, for a given value of solid fraction. The reason for this is the larger grain size given by Equation (3.47), which assumes the grain size varies inversely with the coherency, allowing for higher velocities in this region.

The most important contribution of the coherency may be seen in Figure 4.13c, which shows the velocity and temperature field after 60 seconds. It can be seen here that the fixed particle region first appears, shown by the additional isotherm for better clarity. Like its globular counterpart, there is a significant decrease of the velocity—approximately an order of magnitude—in the fixed particle region due to Darcy damping. However, it is important to note that there is greater penetration of fluid into the fixed particle region for dendritic solidification than globular solidification due to higher permeability of dendritic structures at the coherency point. The lower value of coherency also signals an earlier transition to conduction-dominant heat transfer from convection-dominant.

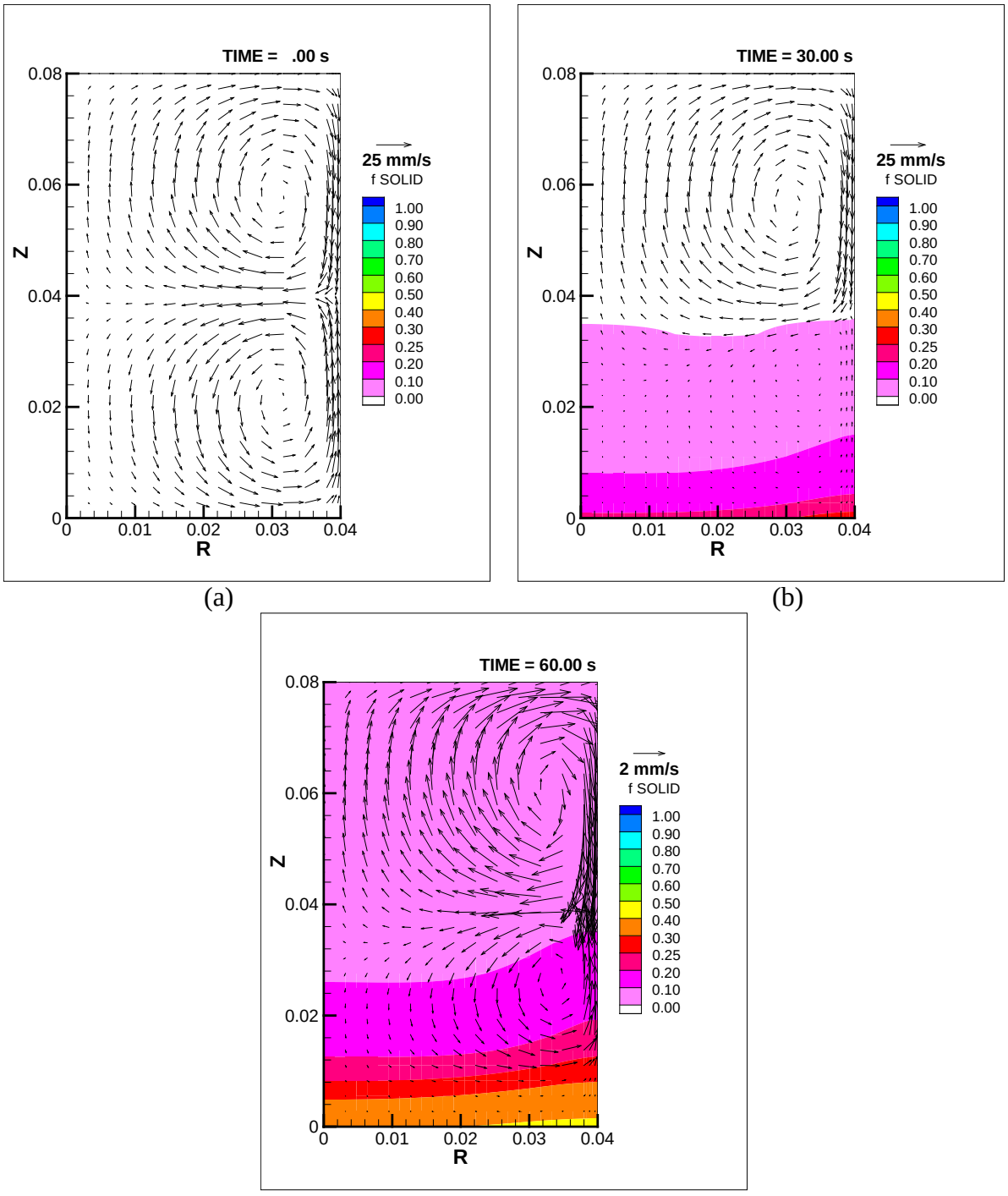

(a) (b)

(c)

Figure 4.13 Velocity and temperature profiles at (a) t=0; (b) t=30; (c) t=60 s

Figure 4.14 shows the evolution of the temperature and velocity fields at later stages of solidification. After 120 seconds (Figure 4.14a), the fixed particle region occupies the bottom third of the metal. The increased penetration depth of the flow can also be better observed in this figure, as it can be seen that the velocity just beyond the coherency isotherm is approximately 1 mm/s and is on the order of 0.3 mm/s at f_s~0.3. This may be contrasted with the characteristic velocity 0.1 mm/s at f_c for globular solidification. It was also found that the velocity becomes nil for $f_s \geq 0.4$. Furthermore, the isotherms in dendritic solidification are relatively in the same position as those of globular solidification, but that the curvature of each isotherm in the fixed particle region is more planar for dendritic solidification, as conduction becomes the primary means of heat transfer more quickly. As the solidification continues in the proceeding figures ($t \geq 240s$), the velocity continues to be nil throughout the metal, similar to globular solidification, until the metal completely solidifies after 504 seconds.

Figure 4.15 shows the evolution of the turbulent kinetic energy during solidification for the case described by Figures 4.13 and 4.14. As expected, the values of the turbulent kinetic energy prior to solidification are the same as those of the globular cases. It is also clear that the turbulence levels continue to mimic those of globular solidification as solidification progresses. This suggests that the value of coherency has no effect on the damping of turbulent kinetic energy, as it occurs at values of solid fraction well below f_c.

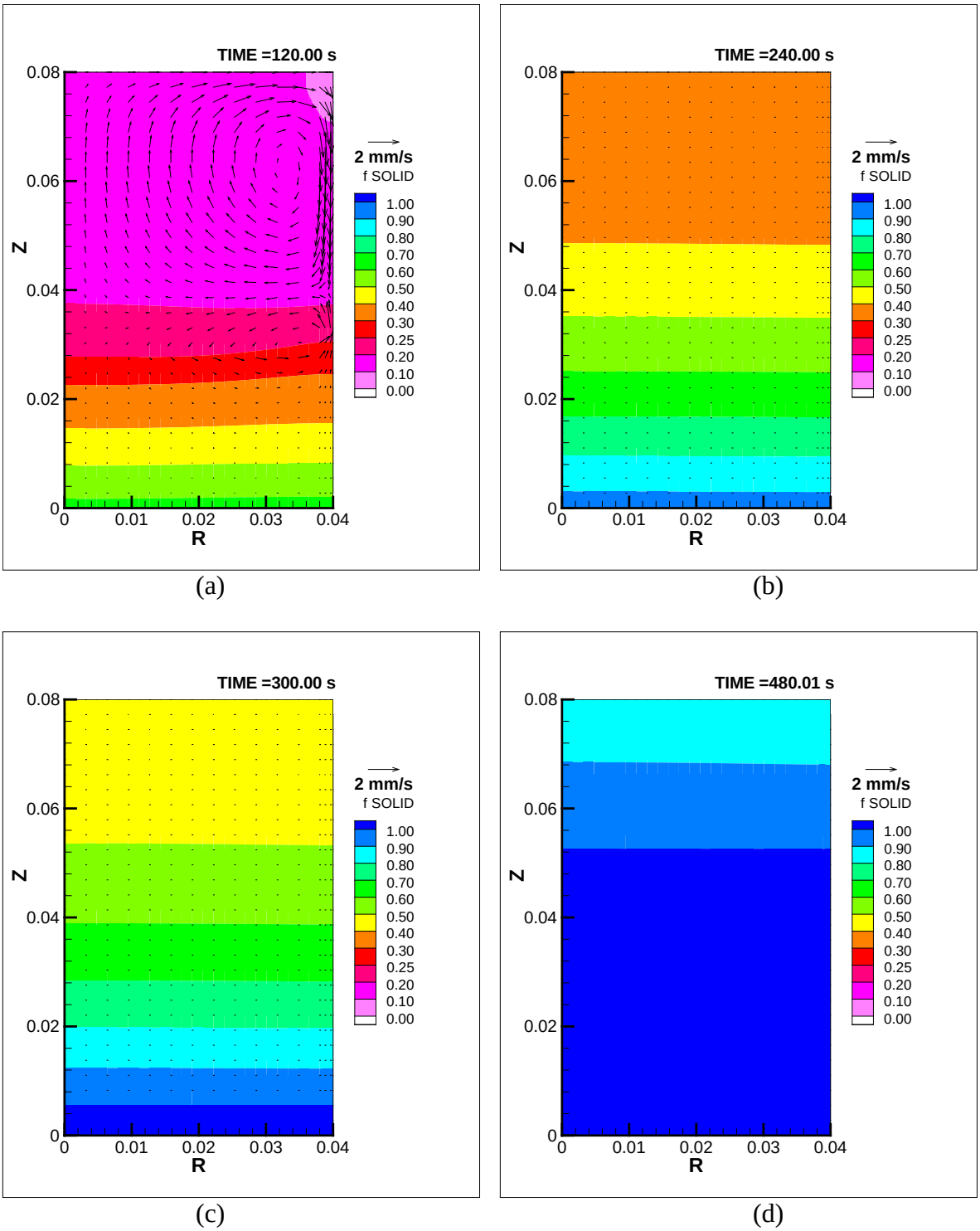

(a) (b)

(c) (d)

Figure 4.14 Velocity and temperature profiles at

(a) t=120; (b) t=240; (c) t=300; (d) t=480 s

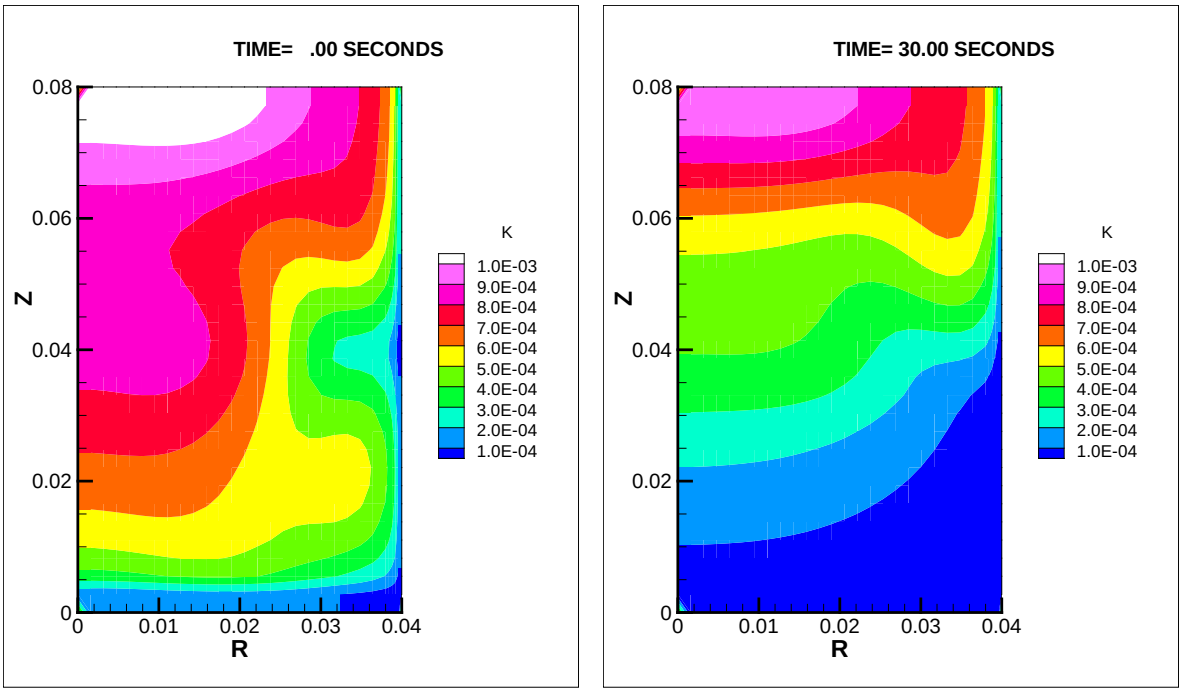

(a) (b)

Figure 4.15 Turbulent kinetic energy profiles at (a) t=0; (b) t=30 s

4.4.2 Effect of Solidification Parameters

Figure 4.16 shows the influence of heat transfer coefficient on solidification of an alloy exhibiting a dendritic morphology. Each cooling curve in this figure was taken at z/H=0.8 and a final grain size of 200 μm. It can immediately be seen that the seconds point of inflection has shifted to T=627°C, which corresponds to an f_s of 0.25 (i.e. the coherency point). It is also found that the solidification times are 929, 455, and 311 seconds for heat transfer coefficient values of 250, 500, and 750 W/m^2-K, respectively. As expected, the solidification times for dendritic morphology are very close to those of globular morphology, as the heat generation and extraction rates are identical given the fact that electrical energy dissipation in the metal is negligible. Figure 4.17 further illustrates the similarity between the globular and dendritic solidification times by plotting them with respect to the Biot number ($Bi=hL/k_s$).

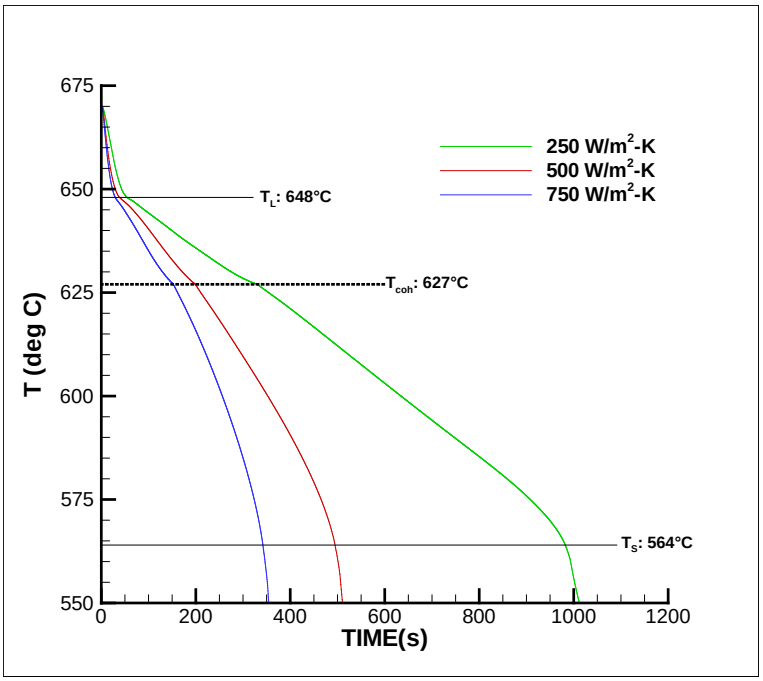

Figure 4.16 Cooling curves for dendritic solidification with variable h

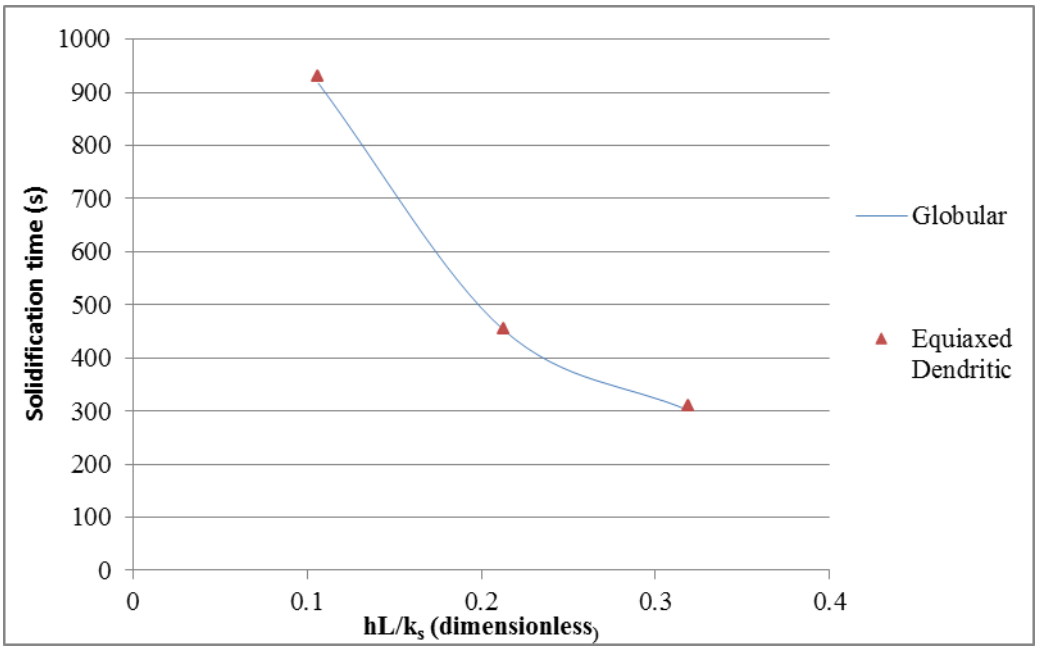

Figure 4.17 Influence of heat transfer coefficient on solidification time

Figure 4.18 shows the influence of the final grain size on the centerline velocity at z/H=0.8. In this figure, it can be clearly seen that the relationship between grain size and velocity for globular solidification (see Figure 4.11) is maintained for dendritic morphology. However, it should be noted that the centerline velocity values are higher for the dendritic morphology, in additional to the lower initial decay rate. This is a result of the more rapid grain growth rate for the dendritic morphology, as it was assumed that the grain size was inversely related to the coherency solid fraction, resulting in lower damping force acting on the fluid in the initial stages of solidification.

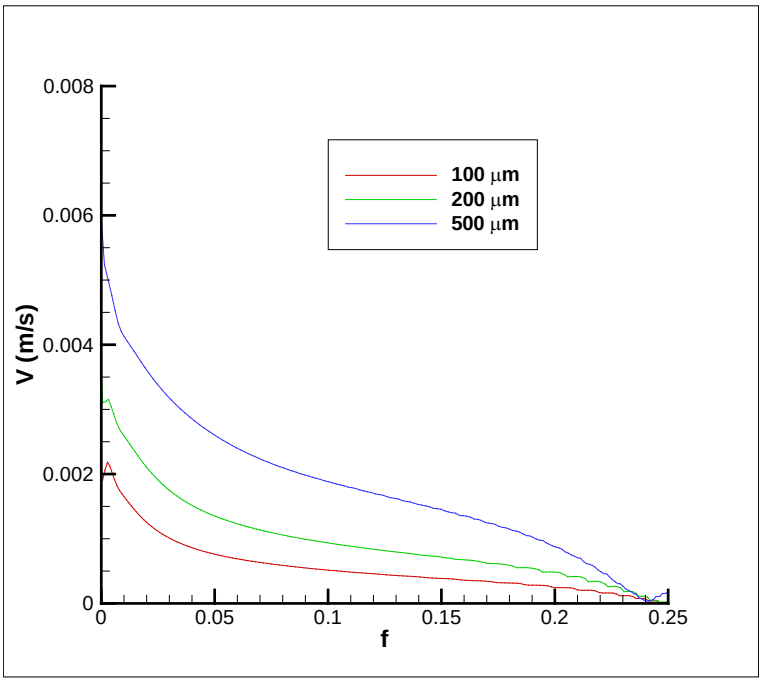

Figure 4.18 Centerline velocity for dendritic morphology for various D_g

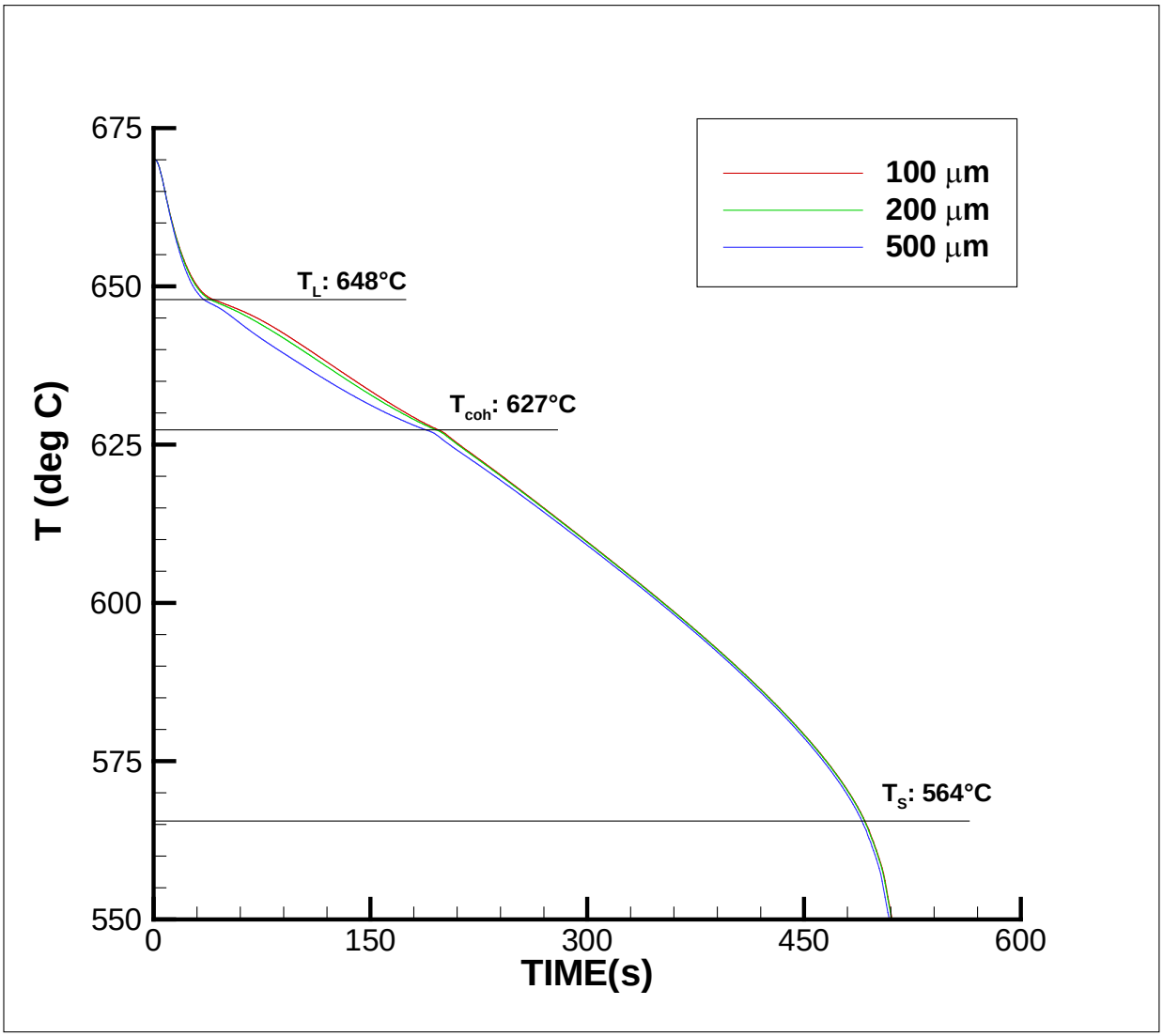

Figure 4.19 Cooling curves for three different D_g with dendritic morphology

Figure 4.19 shows three cooling curves for the three grain sizes investigated at the centerline for z/H=0.8. In general, it can again be seen that the temperature evolution, for both dendritic and globular morphologies, is nearly the same, and that the relationship between the cooling rate and grain size in the suspended particle region continues to hold. It is important to note that unlike the globular cooling curves, there is some noticeable deviation in the cooling curves past the coherency point. This is caused by the increased penetration depth of the flow

into the fixed particle region, making convection still the preeminent mode of heat transfer. This deviation becomes unnoticeable by f_s~0.3 (~620°C), since Darcy damping is significant enough to make the Peclet number—the ratio of convective and diffusive heat transfer—small. The solidification times for each grain size were found to be less than one percent from one another.

CHAPTER 5

CONCLUDING REMARKS AND RECOMMENDATIONS

5.1 Concluding Remarks

1. A model has been developed to describe the electromagnetic and fluid flow phenomena in an EM stirred melt during solidification
2. Flow in the mushy zone was described by dividing it into two regions: The fixed particle region and the suspended particle region. The boundary between these two regions was defined by the coherency solid fraction.
3. Damping of the flow in the suspended particle region occurs through interaction of the turbulent stresses with the crystallite surfaces, while the flow was damped in the fixed particle region by Darcy's law.
4. Calculations were carried out for solidification of the Al-4.5%Cu alloy in a bottom chill mold undergoing linear stirring.
5. It was found that the velocity damping takes place in the initial stages of solidification (f_s<0.1), and the velocity in the suspended particle region was an order of magnitude smaller than that of the bulk liquid.
6. The strength of the damping force was lessened with both larger grain size and small values of coherency solid fraction.

7. Turbulence levels are similarly damped at very low solid fraction, and were found to be negligible after f_s~0.1.
8. Darcian behavior in the fixed particle region further reduced the velocity, with the fluid reaching negligible values a few millimeters below the coherency isotherm. The penetration depth of the flow was shown to increase with lower coherency values.
9. The values of coherency solid fraction and final grain size were shown to have minimal effect on the overall solidification time.
10. The coherency point tends to demarcate the region of solid fraction where the primary mode of heat transfer transitions from convection to conduction.
11. Although the overall solidification rate was unchanged by the coherency value or final grain size, there is local effect on the flow with respect to the suspended particle region. The cooling rate in the initial stages of solidification was shown to increase for larger grain size.

5.2 Recommendations for Future Research

1. Determine the effect of coil geometry, coil current, and coil frequency on the flow structure and intensity in the mushy zone during solidification.
2. Perform experiments to validate the model developed in this work.
3. Expand the model to include mass transfer of the alloying elements to determine predict macro/microsegregation in the final casting.
4. Investigate the effect of coil geometry, coil current, and coil frequency on the evolution of the flow during solidification.
5. Determine the effect of electromagnetic stirring on macro/microsegregation of the cast alloy.

REFERENCES

(1) N El-Kaddah, J Szekely. The turbulent recirculating flow in a coreless induction furnace, a comparison of theoretical predictions with measurements. *J. Fluid Mechanics* 133(1983), 33-46.

(2) AA Tzavaras, HD Brody. Electromagnetic stirring and continuous casting—Achievements, problems, and goals. *JOM* 36(3)(1984), 31-37.

(3) C Vives. New electromagnetic rheocasters for the production of thixotropic aluminum alloy systems. in *Magnetohydrodynamics in Process Metallurgy*. eds. J Szekely, JW Evans, K Blazek, N El-Kaddah (Warrendale: TMS, 1991), 169-174.

(4) VA Kompan, et al. Magnetically controlled electroslag melting of titanium alloys. in *Modeling for Materials Processing*, (Riga, 2010), 85-90.

(5) C Vives, C Perry. Effect of electromagnetic stirring during the controlled solidification of tin. *Int. J. Heat Mass Transfer* 29(1986), 21-33.

(6) L Hachani, et al. Experimental analysis of the solidification of Sn-3wt%Pb alloy under natural convection. *Int. J. Heat Mass Transfer* 55(2012), 1986-1996.

(7) Q Zhao, et al. The effects of electromagnetic stirring on the solidification structure and macrosegregation of Pb-Sn alloy. *Adv. Mater. Res.* 484(2012), 1447-1452.

(8) JA Burton, RC Prim, WP Schlicter. The distribution of solute in crystals grown from the melt—Part I: Theoretical. *J. Chem. Phys.* 21(1953), 1987-1991.

(9) T Takahashi, K Ichikawa, M Kudou. Effect of fluid flow on macrosegregation in steel ingots. *Trans ISIJ*, 16(1976), 283-291.

(10) B Wang, Y Yang, W Tang. Microstructure refinement of AZ91D alloy solidified with pulsed magnetic field. *Trans. Nonferrous Met. Soc. China* 18(2008), 536-540.

(11) B Chalmers. *Principles of Solidification*. (New York: Wiley, 1964)

(12) WC Winegard, B Chalmers. Supercooling and dendritic freezing in alloys. *Trans. Amer. Soc. Metals*, 46(1953), 1214-1224.

(13) Q Han, A Hellawell. Primary particle melting rates and equiaxed grain nucleation. *Met. Mater. Trans. B*, 28(1997), 169-173.

(14) B Chalmers. The structure of ingots. *J. Aust. Inst Metals* 8(1963), 255-263.

(15) B Willers, et al. The columnar-to-equiaxed transition in Pb-Sn alloys affected by electromagnetically driven convection. *Mat Sci Eng A* 402(2005), 55-65.

(16) KA Jackson, JD Hunt, DR Uhlmann, TP Seward III. On the origin of the equiaxed zone in castings. *Trans Met Soc AIME*, 236 (1966), 149-158.

(17) CJ Parides, RN Smith, ME Glicksman. The influence of convection during solidification on fragmentation of the mushy zone of a model alloy. *Met. Trans. A* 28(1997), 875-883.

(18) B Li, HD Brody, A Kazimirov. Real-time observation of dendrite coarsening in Sn-13wt%Bi alloys by synchrotron microradiography. *Phys. Rev. E* 70(2004), 062602.

(19) D Ruvalcaba, et al. In-situ observation of dendrite fragmentation due to local solute-enrichment during directional solidification of an aluminum alloy. *Acta. Mater.* 55(2007), 4287-4292.

(20) JA Dantzig, M Rappaz. *Solidification*. (Lausanne: EPFL Press, 2009).464-466.

(21) J Szekely. The role of software in mathematical modeling. in *Materials Processing in the Computer Age*. eds. VR Voller, MS Stacjpwocz. BG Thomas. (Warrendale: TMS, 1991), 21-34.

(22) SD Ridder, et al. Steady state segregation and heat flow in ESR. *Met. Trans. B* 9(1978), 415-425.

(23) SD Riddler, S Kou, R Mehrabian. Effect of fluid flow on macrosegregation in axisymmetric ingots. *Met. Trans. B* 12(1981), 435-447.

(24) VR Voller, C Prakash. A fixed grid numerical modeling methodology for convection-diffusion mushy region phase-change problems. *Int. J. Heat Mass Transfer* 30(1987), 1709-1719.

(25) WD Bennon, FP Incropera. A continuum model for momentum, heat, and species transport in binary solid-liquid phase change systems—I: Model formulation. *Int. J. Heat Mass Transfer* 30(1987), 2161-2170.

(26) T Campanella, C Charbon, M Rappaz. Influence of permeability on the grain refinement induced by forced convection in copper-base alloys. *Scripta Mater.* 49(2003), 1029-1034.

(27) PC Carman. Fluid flow through granular beds. *Trans. Inst. Chem. Eng.* 15(1937), 150-166.

(28) DR Poirier. Permeability for flow of interdendritic liquid in columnar-dendritic alloys. *Met. Trans. B* 18(1987), 245-255.

(29) W Shyy, et al. Modeling of turbulent transport and solidification during continuous ingot casting. *Int. J. Heat Mass Transfer* 35(1992), 1229-1245.

(30) PJ Prescott, FP Incropera. The effect of turbulence on solidification of a binary metal alloy with electromagnetic stirring. *J. Heat Transfer* 117(1995), 716-724.

(31) Budenkova, et al. Simulation of a directional solidification of a binary Al-7wt%Si and a ternary alloy Al-7wt%Si-1wt%Fe under the action of a rotating magnetic field. *Proc. MCWASP XIII*, IOP Conference Series: *Mat. Sci. Eng.* 33(2012), 012046.

(32) D Apelian, MC Flemings, R Mehrabian. Specific permeability of partially solidified dendritic networks of Al-Si alloys. *Met. Trans.* 5(1974), 2533-2537.

(33) N Streat, F Weinberg. Interdendritic fluid flow in a lead-tin alloy. *Met. Trans. B* 7(1976), 417-423.

(34) R Nasser-Rafi, R Deshmukh, DR Poirier. Flow of interdendritic liquid and permeability in Pb-20wt%Sn alloys. *Met. Mater. Trans. A* 16(1985), 2263-2271.

(35) CM Oldenburg, FJ Spera. Hybrid model for solidification and convection. *Num. Heat Transfer B* 21(1992), 217-229.

(36) CY Wang, S Ahuja, C Beckermann, HC de Groh III. Multiparticle interfacial drag in equiaxed solidification. *Met. Trans. B* 26(1995), 111-119.

(37) J Ni, C Beckermann. A volume-averaged two-phase model for transport phenomena during solidification. *Met. Trans. B* 22(1991), 349-361

(38) J Ni, FP Incropera. Extension of the continuum model for transport phenomena occurring during metal alloy solidification—II: Microscopic considerations. *Int. J. Heat Mass Transfer* 38(1995), 1285-1296.

(39) PA Nikrityuk, K Eckert, R Grundmann. A numerical study of unidirectional solidification of a binary metal alloy under influence of a rotating magnetic field. *Int J Heat Mass Transfer* 49(2006), 1501-1515.

(40) R Pardeshi, AK Singh, P Dutta. Modeling of solidification process in a rotary electromagnetic stirrer. *Num. Heat Transfer A* 55(2008), 42-57.

(41) JD Jackson. *Classical Electrodynamics, 3rd Edition*. (New York: Wiley, 1999).

(42) D Roger, JF Eastham. Finite element solution of 3D eddy current flow in magnetically linear conductors at power frequencies. *IEEE Trans. Magn.* 18(1982), 481-485.

(43) RD Pillsbury. A three dimensional eddy current formulation using two potentials: The magnetic vector potential and total scalar potential. *IEEE Trans. Magn.* 19(1983), 2284-2287.

(44) D Roger, JF Eastham. Multiply connected regions in the A-Y three-dimensional eddy current formulation. *Proc. IEE* 134(1987), 58-66.

(45) MVK Chari, A Konrad, MA Palmo, J D'Angelo. Three dimensional vector potential analysis for machine field problems. *IEEE Trans. Magn.* 18(1982), 436-446.

(46) CS Biddlecombe, EA Heighway, J Simkin, CW Trowbridge. Methods for eddy current computation in three dimensions. *IEEE Trans. Magn.* 18(1982), 492-497.

(47) CJ Carpenter. Comparison of alternative formulations of 3-dimensional magnetic field and eddy-current problems at power frequencies. *Proc. IEE* 124(1977), 1026-1034.

(48) CJ Carpenter, EA Wyatt. Efficiency of numerical techniques for computing eddy currents in two and three dimensions. *Proc COMPUMAG-76* (1976), 242-250.

(49) CJ Carpenter, DH Locke. Numerical models of three-dimensional end winding arrays. *Proc. COMPUMAG-76* (1976), 47-55.

(50) TW Preston, ABJ Reese. Solution of 3-dimensional eddy current problems: The T-Ω method. *IEEE Trans. Magn.* 18(1982), 486-491.

(51) W Reinhart, H Stogner, K Pries. Calculation of 3D eddy current problems by finite element method using either an electric or magnetic vector potential. *IEEE Trans. Magn.* 24(1988), 122-125.

(52) Biro, K Pries. Finite element analysis of 3D eddy currents. *IEEE Trans. Magn.* 26(1990), 418-423.

(53) JN Reddy. *An Introduction to the Finite Element Method.* (New York: McGraw-Hill, 1993).

(54) SV Patankar. *Numerical Heat Transfer and Fluid Flow*. (New York: McGraw-Hill, 1980).

(55) GD Smith. *Numerical Solution of Partial Differential Equations*. (New York: Oxford University Press, 1965).

(56) SJ Salon. The hybrid finite element-boundary element method in electromagnetics. *IEEE Trans. Magn.* 21(1985), 1829-1834.

(57) JL Meyer, N El-Kaddah, J Szekely. A new method for computing electromagnetic force fields in induction furnace. *IEEE Trans. Magn.* 23(1987), 1806-1810.

(58) TT Natarajan, N El-Kaddah. A finite element-integral method for two-dimensional eddy current problems. in *Magnetohydrodynamics in Process Metallurgy*. eds J Szekely, JW Evans, K Blazek, N El-Kaddah. (Warrendale, PA: TMS, 1991). 3-9.

(59) TT Natarajan. An efficient two dimensional FEM/integral method for electromagnetic problems. MS Thesis, University of Alabama, 1991.

(60) E Kolbe, W Reiss. Eine method zur numerische bestimmung der stromdichteverteilung in inductive erwarmten korpen unterschiedlicher geometrisher form. *Wiss. Z der TH Ilmenau* 9(1963), 311-317.

(61) RF Dudley, PE Burke. The prediction of current distribution in induction heating installations. *IEEE Trans. Industry Applications* 8(1972), 565-571.

(62) FW Grover. *Inductance Calculations*. (New York: D Van Nostrand, 1946).

(63) JD Lavers. The influence of system geometry on the electromagnetic stirring forces in crucible induction melting furnaces. in *Metallurgical Applications of Magnetohydrodynamics.* eds HK Moffat, MRE Proctor. (London: The Metals Society, 1984), 62-77.

(64) JL Meyer, J Szekely, N El-Kaddah. Calculation of the electromagnetic field for induction stirring in continuous casting. *ISIJ Intl*. 27(1987), 25-33.

(65) JD Lavers. Computational methods for the analysis of molten metal electromagnetic confinement systems. *ISIJ Intl.* 29(1989), 993-1005.

(66) ERG Eckert, RM Drake. *Analysis of Heat and Mass Transfer*. (New York: McGraw-Hill, 1972).

(67) FC Frank. Radially symmetric phase growth controlled by diffusion. *Proc. Roy. Soc. A* 201(1950), 586-599.

(68) S Paterson. Propagation of a boundary of fusion. *Proc Glasgow Math Assoc* 1(1952), 42-47.

(69) PL Chambre. On the dynamics of phase growth. *Quart. J. Mech. Appl. Math.* 9(1956), 224-233.

(70) TR Goodman. The heat balance integral and its application to problems involving a change in phase. *Trans ASME* 8(1958), 335-342.

(71) NMH Lightfoot. The solidification of steel ingots. *Proc. London Math. Soc.* 31(1929), 97-116.

(72) KA Rathjen, LM Jiji. Heat conduction with melting or freezing in a moving corner. *J Heat Transfer* 93(1971), 101-109.

(73) H Budhia, F Krieth. Heat transfer with melting or freezing in a wedge. *Int J Heat Mass Transfer* 16(1973), 195-211.

(74) LI Rubinstein. *The Stefan Problem*. (Providence: American Mathematical Society, 1971).

(75) WD Murray, F Landis. Numerical and machine solutions of transient heat-conduction problems involving melting or freezing. *J Heat Transfer* 81(1959), 106-112.

(76) SO Unverdi, G Tryggvason. A front-tracking method for viscous, incompressible, multi-fluid flows. *J Comp Phys* 100(1992), 25-37.

(77) S Osher, JA Sethian. Fronts propagating with curvature-dependent speed: Algorithms based on Hamilton-Jacobi formulations. *J. Comp. Phys.* 79(1988), 12-49.

(78) J Crank. Two methods for the numerical solution of moving-boundary problems in diffusion and heat flow. *Quart J Mech Appl Math* 10(1957), 220-231.

(79) JL Duda, MF Malone, RH Notter, JS Vrentas. Analysis of two-dimensional diffusion-controlled moving boundary problems. *Int J Heat Mass Transfer* 18(1975), 901-910.

(80) T Saitoh. Numerical method for multi-dimensional freezing problems in arbitrary domains. *J Heat Transfer* 100(1978), 294-299.

(81) CF Hsu, EM Sparrow, SV Patankar. Numerical solution of moving boundary problems by boundary immobilization and a control-volume-based finite-difference scheme. *Int J Heat Mass Transfer* 24(1981), 1335-1343.

(82) M Lacroix, VR Voller. Finite difference solutions of solidification phase change problems: Transformed grids versus fixed grids. *Num Heat Transfer B* 17(1990), 25-41.

(83) AN Thionov, AA Samarskii. *The Equations of Mathematical Physics, 2nd Ed*. (Moscow: Gittl, 1953).

(84) J Szekely, NJ Thelemis. *Rate Phenomena in Process Metallurgy*. (New York: Wiley, 1971).

(85) BM Budak, EN Sobol'eva, AB Uspenskii. A difference method with coefficient smoothing for the solution of Stefan problems. *Zh Vychisl Mat Mat Fiz* (5)(1965), 828-840.

(86) AA Samarskii, BD Moisynko. An economic continuous calculation scheme for the Stefan multidimensional problem. *Zh Vychisl Mat Mat Fiz* (5)(1965), 816-827.

(87) DM Stefanescu. *Science and Engineering of Casting Solidification, 2nd Ed.* (New York: Springer, 2009). pp. 97-99.

(88) G Poole, N Rimkus, A Murphy, P Boehmcke, N El-Kaddah. Effect of the solidification rate on microstructure of cast Mg alloys at low superheat. in *Magnesium Technology 2012*. eds. SN Mathaudhu, WH Sillekens, NR Neelameggham, N Hort (Warrendale: TMS, 2012), 161-164.

(89) DGR Sharma, M Krishnan, C Ravindran. Determination of the rate of latent heat liberation in binary alloys. *Mater Characterization* 44(2000), 309-320.

(90) CA Siqueira, N Cheung, A Garcia. The columnar to equiaxed transition during solidification of Sn-Pb alloys. *J Alloys and Compounds* 351(2003), 126-134.

(91) KD Carlson, C Beckermann. Determination of solid fraction-temperature relation and latent heat using full scale casting experiments: application to corrosion resistant steels and nickel based alloys. *Int J Cast Metals Research* 25(2012), 75-92.

(92) Y Li, D Apelian, B Xing, Y Ma, Y Hao. Commerical AM60 alloy for semisolid processing: Alloy optimization and thermodynamic analysis. *Trans Nonferrous Metals Soc China*. 20(2010), 1572-1578.

(93) R Trivedi, S Liu, P Mazumder, E Simsek. Microstructure development in directionally solidified Al-4.0wt%Cu alloy system. *Sci Tech Adv Mater* 2(2001), 309-320.

(94) SA Thorpe, PK Hutt, R Soulsby. The effect of horizontal gradients on thermohaline convection. *J Fluid Mech* 38(1969), 375-400.

(95) JE Hart. On sideways diffusive instability. *J Fluid Mech* 99(1971), 279-288.

(96) CF Chen. Onset of cellular convection in a salinity gradient due to a lateral temperature gradient. *J. Fluid Mech.* 63(1974), 563-576.

(97) ME Thompson, J Szekely. Mathematical and physical modeling of double-diffusive convection of aqueous solutions crystallizing at a vertical wall. *J Fluid Mech* 187(1988), 409-433.

(98) HE Huppert, MG Worster. Dynamic solidification of a binary melt. *Nature* 314(1985), 367-384.

(99) MG Worster. Solidification of an alloy from cooled boundary. *J Fluid Mech* 167(1986), 481-501.

(100) W Kurz, DJ Fisher. *Fundamentals of Solidification*. (Rockport, MA: Trans Tech Publications, 1986), 91.

(101) MJ Stewart. Natural Convection in Liquid Metals. PhD Dissertation, University of British Columbia, 1970.

(102) D Brabazon, DJ Browne, AJ Carr. Mechanical stir casting of aluminum alloys from the mushy state: Process, microstructure, and mechanical properties. *Mater Sci Eng A* 326(2002), 370-381.

(103) H Puga. JC Teixeira, J Barbosa, E Seabra, S Ribeiro, M Prokic. The combined effect of melt stirring and ultrasonic agitation on the degassing efficiency of $AlSi_9Cu_3$ alloy. *Mater Lett* 63(2009), 2089-2092.

(104) SF Liu, LY Liu, LG Kang. Refinement role of electromagnetic stirring and strontium in AZ91 magnesium alloy. *J. Alloys Compounds* 450(2008) 546-550.

(105) AV Kuznetsov. Investigation of the coupled heat transfer, fluid flow, and the solute transport during the strip casting process. *Int J Heat Mass Transfer* 40(1997), 2949-2961.

(106) TS Piwonka, MC Flemings. Pore formation in solidification. *Trans Met Soc AIME* 236(1966), 1157-1165.

(107) R Mehrabian, M Keane, MC Flemings. Interdendritic fluid flow and macrosegregation: Influence of gravity. *Met. Trans.* 1(1970), 1209-1219.

(108) R Mehrabian, M Keane, MC Flemings. Macrosegregation in ternary alloys. *Met Trans* 1(1970), 455-464.

(109) J Szekely, AS Jassal. An experimental and analytical study of the solidification of a binary dendritic system. *Met. Trans. B* 9(1978), 389-397.

(110) S Ganesan, CL Chan, DR Poirier. Permeability for flow parallel to primary dendrite arms. *Mater. Sci. Eng. A* 151(1992), 97-105.

(111) RB Bird, WE Stewart, EN Lightfoot. *Transport Phenomena*. (New York: Wiley, 1960), pp 196-200.

(112) S Kou, DR Poirier, MC Flemings. Macrosegregation in rotated remelted ingots. *Met. Trans. B* 9(1978), 711-719.

(113) S Felicelli, JC Heinrich, DR Poirier. Simulation of freckles during vertical solidification of binary alloys. *Met. Trans. B* 22(1991) 847-859.

(114) AL Maples, DR Poirier. Convection in the two-phase zone of solidifying alloys. *Met. Trans. B* 15(1984), 163-172.

(115) K Murakami, A Shiraishi, T Okamoto. Interdendritic fluid flow normal to primary dendrite arms in cubic alloys, *Acta Metall.* 31(1983), 1417-1424.

(116) K Murakami, T Okamoto. Fluid flow in interdendritic space in cubic alloys. *Acta Metall* 32(1984), 1423-1428

(117) RG Santos, MLNM Melo. Permeability of interdendritic channels. *Mater. Sci. Eng. A* 391(2005), 151-158.

(118) HC de Groh III, PD Weidman, R Zakhem, S Ahuja, C Beckermann. Calculation of a dendrite settling velocities using a porous envelope. *Met Trans B* 24(1993), 749-753.\

(119) H Danon, M Wolfshtein, G Hetsroni. Numerical calculations of two-phase turbulent round jet. *Int. J. Multiphase Flow* 3(1977), 223-234.

(120) WP Jones, BE Launder. The prediction of laminarization with a two-equation model of turbulence. *Int. J. Heat Mass Transfer* 15(1972), 301-314.

(121) H Tennekes, JL Lumley. *A First Course in Turbulence*. (Cambridge, MA: MIT Press, 1972).

(122) R West. On the permeability of the two-phase zone during solidification of alloys. *Met. Trans. A* 16(1985), 693.

(123) S Chang, DM Stefanescu. A model for macrosegregation and its application to Al-Cu castings. *Met. Trans. A* 27(1996), 2708-2721.

(124) OJ Ilegbusi, MD Mat. Modeling flowability of the mushy zone with a hybrid model utilizing coherency solid fraction. *Mater. Sci. Eng. A* 247(1998), 135-141.

(125) MD Mat, OJ Ilegbusi. Application of a hybrid model of mushy zone to macrosegregation in alloy solidification. *Int. J. Heat Mass Transfer* 45(2002), 279-289.

(126) BE Launder, DB Spalding. *Mathematical Models of Turbulence*. (London, Academic Press, 1972).

(127) M Mooney. The viscosity of a concentrated suspension of spherical particles. *J Colloid Science* 6(1951), 162-170.